Journal of Water Process Engineering 50 (2022) 103248

Contents lists available at ScienceDirect

Journal of Water Process Engineering

journal homepage: www.elsevier.com/locate/jwpe

Graphene oxide-safranin modified@polyacrylonitrile membranes for water purification: Reuse and mechanism based on theoretical calculations and XPS analysis

Tauany de Figueiredo Neves [a], Natália Gabriele Camparotto [a], Giani de Vargas Brião [b], Valmor Roberto Mastelaro [c], Renato Falcão Dantas [a], Melissa Gurgel Adeodato Vieira [b], Patrícia Prediger [a,*]

[a] Limeira School of Technology, University of Campinas, PO Box 456, 13484-332 Limeira, S.P., Brazil
[b] Campinas School of Chemical Engineering, University of Campinas, PO Box 6066, 13083-852 Campinas, S.P., Brazil
[c] São Carlos Institute of Physics, University of São Paulo, PO Box 369, 13566-590 São Carlos, S.P., Brazil

ARTICLE INFO

Keywords:
Polymeric membranes
Functionalized graphene oxide
Complex dyes
Adsorption
Density functional theory

ABSTRACT

The difficulty in metabolizing and degrading complex dyes containing three or more aromatic rings ascends new alternatives in the treatment of colored water, including adsorption. Despite advances in this area, the adsorption of complex dyes has been little reported. In this work, polyacrylonitrile membranes incorporated with graphene oxide functionalized with safranin dye (hPAN@GO-SF) were applied to remove the complex cationic dyes basic blue 7 (BB7) and basic brown 4 (BB4), and the anionic direct black 22 (DB22) from water. The advantage of using nanoadsorbents immobilized on polymeric membranes is their easy removal after adsorption. Under the best conditions established for dye removal, high adsorption capacities of 1143/1035, 873/799 and 205/148 $mg{\cdot}g^{-1}$ were achieved for BB4, BB7 and DB22 in the single and saline system, respectively. Henry and Temkin's isothermal models best fitted equilibrium experimental data of dyes in single and saline systems, respectively, while the kinetic model of intraparticle diffusion fitted well the empirical data in both systems. Furthermore, hPAN@GO-SF can be used for five consecutive cycles without loss of efficiency for the BB7 dye. Theoretical calculations and post-adsorbed membrane analyses showed that the adsorbent/adsorbate interactions are based on H-bonding, π-π and electrostatic interactions.

1. Introduction

Textile and clothing industries are one of the main socio-economic pillars of lower-middle income countries. Allied with the growth of this sector, the presence of dyes in wastewater becomes recurrent [1]. Synthetic dyes, industrially preferred to natural dyes, are classified according to their chemical properties, such as azo, triarylmethane, phthalocyanine, anthraquinone, and sulfur dyes [2]. The more complex the dye, the more difficult it is to decompose. Thus, the so-called complex dyes, substances with more than three aromatic rings, are considerably more difficult to degrade and can produce toxic metabolites [3].

The cationic dyes basic blue 7 (BB7, triarylmethane dye, Fig. 1a) and basic brown 4 (BB4, azo dye, Fig. 1b), and the anionic dye direct black 22 (DB22, azo dye, Fig. 1c) are some of the complex dyes commonly used in the dyeing of natural fibers and polymeric fibers [4]. Despite their wide applications, these recalcitrant organic contaminants usually are considered toxic, mutagenic and carcinogenic and when in hydric bodies, may obstruct the sunlight passage and reduce oxygen solubility [5]. Therefore, the toxicological potentials and the resistance of dyes to degradation represent a central challenge for complex dyes removal technologies.

Due to the complexity of their structures, the removal of these dyes from water has been little explored, with chemical methodologies, such as photocatalysis, oxidation, and ozonation, being the most studied. However, these complex and expensive processes can generate by-products that are more toxic than the starting materials [6]. Thus, the scientific community has shown great interest in treating of colored waters by adsorptive processes, given the technique's advantages [7].

Adsorption, a mass transfer phenomenon in which adsorptive molecules accumulate on the interlayer of a liquid and solid phase, is a

* Corresponding author.
E-mail address: prediger@unicamp.br (P. Prediger).

https://doi.org/10.1016/j.jwpe.2022.103248
Received 29 August 2022; Received in revised form 11 October 2022; Accepted 12 October 2022
Available online 20 October 2022

simple technique, with low execution and maintenance costs and a high removal rate. The adsorbent/adsorbate interactions involve chemical and physical processes, so the technique's performance is strictly linked to the sorbent materials used. These materials must have an extensive surface area, selectivity, high adsorption potential, and recyclability potential [8]. Among the various adsorbent materials used in the treatment of colored water, graphene oxide (GO) stands out. GO is a nanoadsorbent derived from the incomplete oxidation of graphite. Given its nanosheets structure of sp^2 hybridized carbons with carboxyl, hydroxyl and epoxide groups on the sheets, it can interact with organic compounds and metallic ions [9].

Despite the adsorptive potential of GO, studies have shown that its adsorbent character can be enhanced by functionalization. Neves et al. [10] grafted GO with quaternary ammonium salt to prepare a new adsorbent with capacity of stripping BB4 dye from water. The maximum removal potential of the mCS/GO-QAS adsorbent was about 650 $mg{\cdot}g^{-1}$. Although several studies have demonstrated the preparation and application of new GO-based nanomaterials, there is a limiting factor regarding the difficulty of removing the adsorbent from water after use. Proposals such as immobilization of GO in polymeric structures and preparation of magnetic adsorbents are some of the alternatives reported in recent years [11]. Among the techniques, GO immobilization in polymeric membranes stands out for combining two technologies in the treatment of colored water: separation and adsorption [12].

Zhu et al. [13] reported the significant potential for retention of the reactive dyes, reactive red 49 (97.2 %) and black 5 (99.2 %), by polyethersulfone loose nanofiltration membrane incorporated with GO functionalized by poly(sulfobetaine methacrylate) (PES/GO-PSBMA). The use of GO incorporated into polymeric membranes for adsorption of dyes in batch assays was reported once by Das et al. [14]. They immobilized chitosan and graphene oxide into polyvinyl alcohol membrane-like adsorbents and used it in congo red dye adsorption. However, high dose of the adsorbent was required and consequently low congo red dye adsorption capacity was achieved, remaining at 12 $mg{\cdot}g^{-1}$.

Recently, we showed that polyacrylonitrile membranes incorporated with GO (hPAN@GO) and GO functionalized with safranin (SF) dye (hPAN@GO-SF) [15] had great potential for removal of multiple contaminants in water. Even under non-optimal conditions, with adsorption capacities of 246.7 and 225.6 $mg{\cdot}m^{-2}$ for basic green 4 and basic blue 26 dyes, respectively, in continuous flow and of 200.6, 191.1 and 154.8 $mg{\cdot}g^{-1}$ for propranolol pharmacological drug, methylene blue dye and benzalkonium chloride surfactant, respectively, in batch assays. In this study [15], we could conclude that the adsorbate's flow profile directly influences the polymeric membranes' selectivity. Therefore, despite advances in this area, the adsorption of complex dyes on polymeric membranes incorporated with functionalized GO has not been explored in batch assays, and the adsorbent/adsorbate interaction mechanisms have not been studied.

Thus, the goal of the current research was to investigate the removal potential of the cationic complex dyes BB7 and BB4 and the anionic complex dye DB22 by the hPAN@GO-SF membrane in batch studies and to delineate the mechanisms that govern the interactive membrane/complex dyes process. Therefore, parameters such as solution pH, adsorbent/adsorbate contact time, nanomaterial content in the membrane, membrane amount, dye concentration and medium temperature parameters were analyzed. The membrane adsorption potential for complex dyes was also explored in saline medium, and the regenerative ability of hPAN@GO-SF was evaluated in consecutive cycles of adsorption. Meanwhile, kinetic and isotherm models were employed to assess the adsorbent/adsorbate interactions in single system and in the presence of interfering agents. Furthermore, studies of the membrane/complex dyes interactive mechanisms were based on FTIR, SEM and XPS analyses of the membranes post adsorptive process and on density functional theory (DFT) calculations, a tool used to detail quantum systems of molecules in the ground state and relate it to the reactivity to adsorption on solid surfaces.

2. Experimental section

Information regarding this topic is presented in the supplementary material. It includes the reagents and methodologies utilized for the membranes preparation and descriptions of the adsorption assays and the studies performed.

3. Results and discussion

3.1. Characterizations

In previous work [15], hPAN@GO-SF membranes were prepared and characterized. A summary of the results of the characterizations performed, is shown in Table 1.

In a previous work [15], removal tests for multiple contaminants in water were performed to evaluate how GO and GO-SF influenced the polyacrylonitrile polymer (PAN) adsorption capacity. The results indicated that incorporating GO and GO-SF into the polymeric matrix has provided morphological and chemical-physical modifications to the pristine membrane, enhancing the adsorptive character of hPAN. Among the evaluated contaminants, the new membranes stood out from the hPAN@GO and hPAN membranes for the cationic dyes BB7 and BB4 and for the anionic one DB22. Thus, the three contaminants were selected to investigate the adsorptive potential and the interactive mechanisms of hPAN@GO-SF membranes.

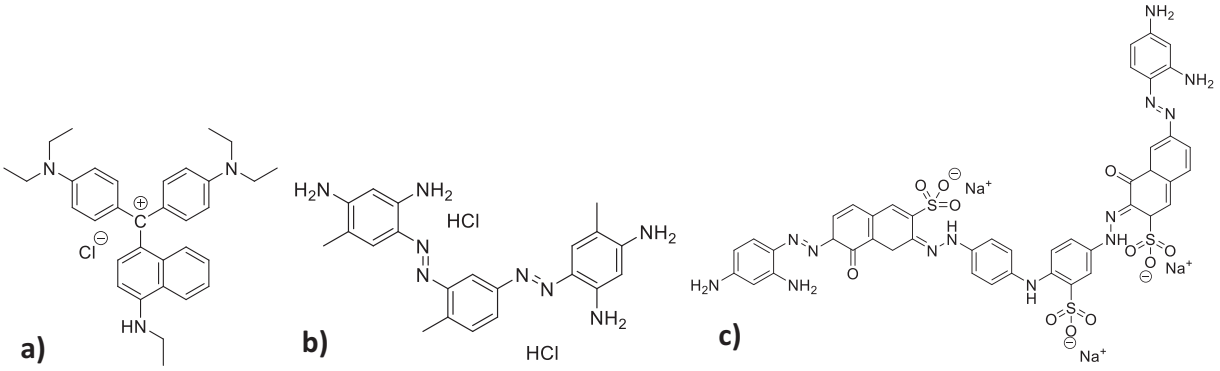

Fig. 1. a) BB7, b) BB4 and c) DB22 molecular structure.

Table 1
hPAN@GO-SF summary characterizations (analysis data not shown).

hPAN-GO-SF	
FT-IR	There was a reduction in the intensity of the bands referring to the hydrolyzed polymer according to the increase of GO-SF in the matrix.
XPS	The presence of GO-SF in the membranes was confirmed by the increase in N content and appearance of chlorine in the elemental composition of hPAN@GO-SF. The high resolution C1s spectrum indicated peaks referring to C-sp^3/ C-sp^2 (284.2 eV), C-N/C-O (285.1 eV), C-O-C (286.1 eV), C═O (287.2 eV) and COOH (288.0) and high resolution N1s spectrum indicated peaks referring to NH_2 (399.2 eV) and N-C═O/N ≡ C (399.9 eV).
Morphological Properties	hPAN@GO-SF showed asymmetrical and narrower fingers-like macrovoids sublayer, less rough surface and higher VOI and pores volume.
Water contact angle	hPAN@GO-SF was more hydrophilic than hPAN@GO, due to the incorporation of SF dye, which contains two amino and one phenazinium groups in its structure.
Pure water flux (PWF)	hPAN@GO-SF showed higher PWF 127.38 $L{\cdot}m^{-2}{\cdot}h^{-1}$ related to its permeability and morphological properties.
Zeta potential	The incorporation of GO-SF into the hPAN membrane provided a less negative surface charge compared to the hPAN@GO membranes. For hPAN@GO-SF 6 % the zeta potential was −25.85, −35.5, −40.57 and − 42.2 mV for pH 4, 6, 8 and 10.

3.2. Adsorption performances of BB7, BB4 and DB22 dyes onto hPAN@GO-SF

3.2.1. Initial pH effects

Adsorption assays were performed at various initial pHs (Fig. 2a) to evaluate the influence of pH on the adsorption of dyes through the hPAN@GO-SF membrane. For BB4 and DB22 dyes, the pH ranged from 2 to 12, while for BB7 dye, the maximum pH was 8 due to its insoluble character under basic conditions [4].

The adsorbent/adsorbate interactions for the three contaminants were pH dependent (Fig. 2a). Concerning the BB7 dye (Fig. 2a), the hPAN@GO-SF membrane provided lower adsorption at pH 2, about 48.7 $mg{\cdot}g^{-1}$. This may be associated with protonation of the membrane nitrogen and oxygen based-functions, which increased the zeta potential (Table 1), reducing the electrostatic attractions with the cationic dye. The microspecies of BB7 dye according to pH are shown in Fig. S2a and indicate the presence of positively charged molecules at pH 2. At pH 4 and 8, the adsorption potentials of BB7 were similar, 145.2 and 132.7 $mg{\cdot}g^{-1}$, respectively. At pH 4, despite being less electronegative than at higher pH, the hPAN@GO-SF membrane has an estimated surface charge of −25.8 mV (Table 1) while the average charge of BB7 species is 2.8 (Fig. S2a). At pH 8, the membrane surface charge dropped to −40.6 mV (Table 1) and dye molecules decreased to 1.0 (Fig. S2a). In both cases, differences between adsorbent/adsorbate charges may have generated attractive forces, as indicated by the results (Fig. 2a). At pH 6, where the highest adsorption potential of the membrane was observed (173.2 $mg{\cdot}g^{-1}$), the average charge of the dye species present in the medium is 1.03 (Fig. S2a), while hPAN@GO-SF has a decreased surface charge of −35.5 mV (Table 1), compared to basic conditions. Although the differences between the charges are similar to those estimated at pH 8, at pH 6 the presence of di-cationic dye species (Fig. S2a), not present at the most basic pH, may contribute to a more significant adsorbent/adsorbate interaction. Thus, as the electrostatic attraction forces are higher at pH 6 than at other pHs, there is closer proximity adsorbent/adsorbate, which enables and potentiates H-bonding and π-π interactions.

Regarding BB4 dye (Fig. 2b), the hPAN@GO-SF membrane showed lower adsorption capacities at pH 2, 10 and 12, median adsorption capacities at pH 4 and 8, and the highest value at pH 6. As for BB7, at pH 2, the membrane exhibited a low adsorption potential of 28.0 $mg{\cdot}g^{-1}$, due to the protonation of the hPAN@GO-SF functional groups and the average charge of BB4 species of 2.0 (Fig. S2b), which results in electrostatic repulsions between adsorbent/adsorbate. At pH 10 and 12, the low adsorption potentials of 85.1 and 73.7 $mg{\cdot}g^{-1}$ are associated to the loss of stability of the dye molecules due to the excess of OH^- ions in the medium [16]. At pH 6, the highest membrane adsorbent potential was observed (150.3 $mg{\cdot}g^{-1}$). In this case, due to the neutrality of the medium, the dye molecules tend not to precipitate as in basic pH, allowing greater adsorbent/adsorbate interactions. Also, considering that in this pH range, although the hPAN@GO-SF membrane has an electronegative charge surface (−35.5 mV) (Table 1), the dye species in the medium have no charge (Fig. S2b) and electrostatic forces of attraction can occur between an electrified object and a neutral object [17]. Furthermore, as the membrane is endowed with oxygenated and nitrogenous groups, in addition to the dye composed of NH_2, hydrogen bond can also occur [18], further enhancing the π-π and electrostatic interactions between the hPAN@GO-SF and dye. At pH 4 and 8, membrane adsorption potentials were similarly expressed, 120.1 and 117.4 $mg{\cdot}g^{-1}$, respectively. At pH 4, opposite charges of hPAN@GO-SF (−25.8 mV) (Table 1) and dye molecules (0.3) (Fig. S2b) generate electrostatic attraction between them, enhancing the adsorbent/adsorbate interactions. In turn, at pH 8, the presence of OH^- in the solution, albeit at a smaller concentration than in the higher pH ranges, reduces the stability of the dye, thus decreasing the membrane adsorption capacity compared to pH 6 [10].

Regarding DB22 dye (Fig. 2c), the highest membrane adsorptive potential of 71.8 $mg{\cdot}g^{-1}$ was obtained at pH 2, where most dye microspecies have charges equal to −1 (Fig. S2c), which reduces the electrostatic repulsive forces between adsorbent/adsorbate. Furthermore, as the dye and membrane have nitrogen and oxygen groups, hydrogen bonds may also be present in the process [4], favoring other interactions in the system. The decrease in membrane adsorptive potential from 71.8 to 2.2 $mg{\cdot}g^{-1}$ with increasing pH (2−12) was related to an increase of OH^- in the medium, which deprotonates the functional groups of DB22 and hPAN@GO-SF, providing negative charges to the dye and the membrane. Thus, increased electrostatic repulsive forces between adsorbent/adsorbate result in a decrease in membrane adsorption capacity.

Therefore, according to the pH assays, pH 6 was best established for the dyes BB7 and BB4, and pH 2 for the dye DB22.

3.2.2. Contact time effects

The adsorbent/adsorbate contact time influence on the process of dye removal by the hPAN@GO-SF membrane was evaluated with aliquots collected in the time interval of 0.0083–26 h (Fig. 2b). The results obtained indicated that the three dyes showed similar behavior over time. Initially, there was a progressive increase in the adsorption potential over time, with maximum potential reached in 12 h, followed by stabilization of the interactive process. For BB7 and BB4, hPAN@GO-SF showed higher equilibrium adsorption capacities of 178,6 $mg{\cdot}g^{-1}$ and 150.0 $mg{\cdot}g^{-1}$, respectively. Regarding DB22 dye, the adsorption capacity was 71.1 $mg{\cdot}g^{-1}$, probably due electrostatic repulsion between the membrane and dye, both negatively charged.

The differences observed between the adsorption potentials of hPAN/GO-SF for the BB7 and BB4 in relation to the DB22 are associated with the surface charges of the membrane and dye species. Despite having a fenazinium cation due to the SF, hPAN@GO-SF has a negative surface charge, which contributes to attractive electrostatic interactions between the membrane and the cationic dyes and repulsive forces between the membrane and the anionic dye [19]. The proximity between the membrane and the BB7 and BB4 dyes, mediated by attractive forces, facilitates H-bonding and π-π adsorbent/adsorbate interactions [20]. On the other hand, the distance due to the electrostatic repulsions between the DB22 dye and the hPAN@GO-SF membrane hinders the other interactions between contaminant and adsorbent, expressed by the lower adsorptive capacity of the membrane.

Furthermore, the differences between the adsorption capacities of both cationic dyes, from 178.6 $mg{\cdot}g^{-1}$ (0.35 mmol/g, Fig. 2b) and 150.0

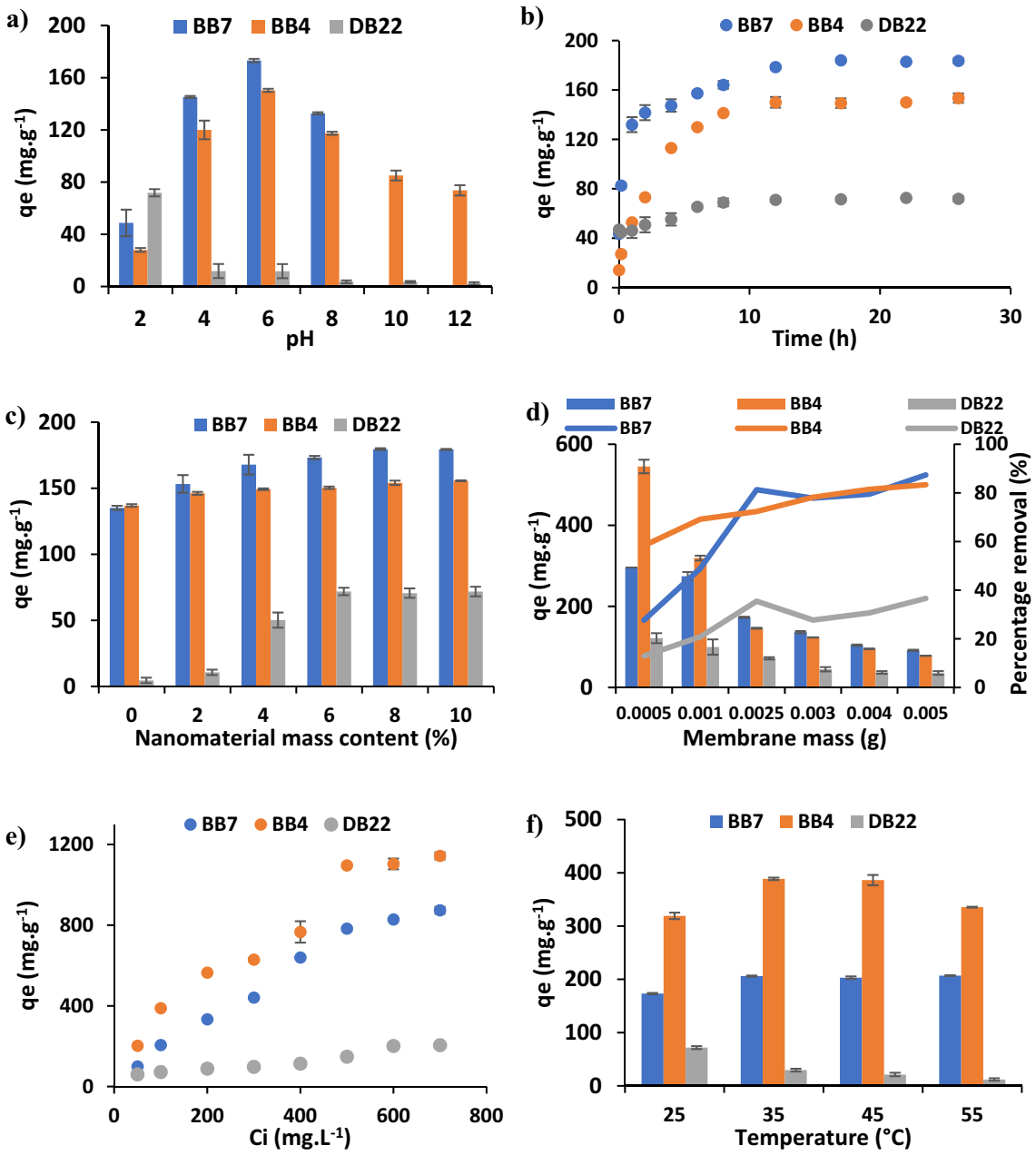

Fig. 2. a) Initial pH variation from 2 to 8 for BB7 and 2 to 12 for BB4 and DB22. b) Variation in dyes uptake overtime from 0 to 24 h. c) GO-SF content in membrane range 2 to 10 %. d) Membrane mass variation from 0.0005 to 0.005 g. e) Initial dyes concentration variation from 50 to 700 mg·L^{-1}. f) Temperature variation from 25 to 55 °C. Optimized conditions, to BB7: Nanomaterial content 6 %, membrane mass: 0.0025 g, 100 mg·L^{-1} of dyes initial concentration, pH 6 and at 35 °C, to BB4: Nanomaterial content 2 %, membrane mass: 0.001 g, 100 mg·L^{-1} of dyes initial concentration, pH 6 and at 35 °C and to DB22: Nanomaterial content 6 %, membrane mass: 0.0025 g, 100 mg·L^{-1} of dyes initial concentration, pH 2 and at 25 °C.

mg·g^{-1} (0.32 mmol/g, Fig. 2b) for BB7 and BB4, respectively, may be related to the amount of aromatic rings in each molecule. While BB7 dye has four aromatic structures, BB4 dye has three. Previous studies have shown that π-π interactions are some of the strongest present between adsorbent/adsorbate in adsorptive systems [21]. Thus, as BB7 has more aromatic rings than BB4 contributes to greater π-π interactions between membrane and BB7 [18].

As the equilibrium in dye removal by hPAN@GO-SF was reached, on average, in 12 h, the other experiments of the optimization process were performed within this time interval.

3.2.3. *Effect of nanomaterial content on the hPAN@GO-SF membrane*

The adsorbent dosage on the membrane and its relation to dye adsorption was evaluated by varying the GO-SF content from 0 to 10 % (w/w) (Fig. 2c). For all three dyes, the results showed that embedding GO-SF into hPAN membranes improves the adsorptive capacity of the material, with qe variating 135.1–179.3 mg·g^{-1}, 136.9–155.6 mg·g^{-1} and 4.5–71.8 mg·g^{-1} for the dyes BB7, BB4 and DB22, respectively. For the three dyes evaluated, up to the incorporation of 6 % by mass of GO-SF in hPAN, there is a progressive rise in the adsorption capacity of the new membranes, and, subsequently, a stabilization of the material's adsorption capacity.

This higher efficiency is related to the increase in the adsorbent/adsorbate contact surface and the higher amount of active sites on the material due to the incorporation of GO-SF in the membrane [22]. The stabilization of the membrane adsorbent system after the addition of >6

% of GO-SF in the material is associated with the unsaturation of the interaction centers of the spare adsorbent in the membrane [23] or even due to the clustering of GO-SF, which, by forming conglomerates, reduces the membrane/dye contact surface [24]. Thus, the optimized GO-SF content was 6 % for BB7 and DB22 dyes, and 2 % for BB4 dye.

3.2.4. Influence of membrane mass variation

The dye adsorption performance of the new membranes concerning their mass was evaluated with variations from 0.0005 g to 0.005 g of material in 5 mL of dye solution, and the evolution of hPAN@GO-SF adsorption potential for the three dyes can be seen in the Fig. 2d. Overall, for all dyes evaluated, the membranes showed similar adsorption profiles. There was a gradual decline in the membrane adsorption potential and a progressive rise in the contaminant percentage removal with increasing hPAN@GO-SF mass.

When the initial membrane mass was 0.0005 g, higher qe and lower removal rate were obtained for the three dyes, around 295.3 $mg{\cdot}g^{-1}$ (27.7 %), 545.1 $mg{\cdot}g^{-1}$ (58.3 %) and 121.6 $mg{\cdot}g^{-1}$ (12.9 %) for BB7, BB4 and DB22, respectively. In turn, for the mass of 0.005 g these values decreased for qe and increased for percentage removal, around 91.5 $mg{\cdot}g^{-1}$ (83.3 %), 78.3 $mg{\cdot}g^{-1}$ (87.5 %) and 35.7 $mg{\cdot}g^{-1}$ (36.6 %) for BB7, BB4 and DB22, respectively. The adsorption capacity, an inherent characteristic of the material, is related to the number of interactive centers available in the substrate after the tests. Furthermore, the percentage removal is related to how much of the total contaminant is adhered to the substrate after the adsorptive process. Therefore, the more the unsaturated interaction centers after the adsorptive process, the lower the material's adsorption capacity [25] and the greater the amount of adsorbate molecules adhered to the solid [26]. For the assay, the greater availability of interactive centers in the adsorbent according to the rise in the material mass, results in an increase in unsaturation of interaction centers and contaminating molecules adhered to hPAN@GO-SF.

As these amounts are inversely proportional, the choice of the mass of membranes to be used in the subsequent assays must consider good qe and percentage removal. Thus, for the BB7 and DB22 dyes, the optimized hPANGO-SF membrane mass was 0.0025 g and for the BB4 dye it was 0.001 g.

3.2.5. Dye concentration effects

The effect of the initial dye content on the adsorption capacity of hPAN@GO-SF was evaluated by ranging the concentration of BB7, BB4 and DB22 dyes from 50 to 700 $mg{\cdot}L^{-1}$, and the results obtained are presented in Fig. 2e.

The membrane adsorptive potential for the three dyes (Fig. 2e) increased with the increment of contaminant in the medium, up to the material saturation around the concentration of 600–700 $mg{\cdot}L^{-1}$. In these plateaus, the adsorption capacity of hPAN@GO-SF was 873.7 (1.7 $mmol{\cdot}g^{-1}$), 1143.1 (2.5 $mmol{\cdot}g^{-1}$) and 204.9 $mg{\cdot}g^{-1}$ (0.2 $mmol{\cdot}g^{-1}$) for BB7, BB4 and DB22 dyes, respectively.

As previously discussed, the increase of the adsorption potential of the membranes is related to the saturation of the active sites available in the solid after the adsorption process [10]. In this case, the rise in the content of contaminant molecules in the solution culminates in the filling of the interactive centers of the membrane, until its complete saturation from 600 $mg{\cdot}L^{-1}$ of dye. Thus, the initial concentration of 100 $mg{\cdot}L^{-1}$ of dyes was estimated for the other tests.

3.2.6. Effect of temperature variation

The effect of temperature on the adsorption capacity of hPAN@GO-SF membranes was evaluated by ranging the system temperature from 25 to 55 °C (Fig. 2f). The membrane adsorption efficiency for cationic dyes increases up to 35 °C, from 173.2 to 206.2 $mg{\cdot}g^{-1}$ and from 319.2 to 388.7 $mg{\cdot}g^{-1}$ for BB7 and BB4, respectively, and remains constant up to 55 °C for the former and decays to 335.5 $mg{\cdot}g^{-1}$ for the latter. As for DB22 dye, the higher the temperature, the lower the membrane adsorption capacity, ranging from 71.8 to 11.9 $mg{\cdot}g^{-1}$ for the temperature range from 25 to 55 °C, respectively.

The adsorption of organic substances depends substantially on the water solubility of these compounds [27] and the increase in temperature causes an increase in the kinetic energy and mobility of the dyes, promoting greater solubility and chemical potential of the compound [28]. This conformity may be indicative of the endothermic process observed for the BB7 dye (Fig. 2f). The temperature rise increased the diffusion rate of the dye up to the interactive sites of the material, a relationship attributed to the weakening of H-bonding between solvent, adsorbate and adsorbent [27]. For BB4 dye, this same profile was observed with growing temperatures from 25 to 35 °C. However, the decay of the membrane's adsorption capacity at higher temperature ranges suggests that another process may be taking place. Previous studies [4] indicated that at higher temperatures, there is an increase in the oscillatory energy of molecules adsorbed on solid surfaces due to the rise in the medium energy, sufficient to supply the interactive adsorbent/adsorbate forces, facilitating the migration of contaminant molecules to the surface solution. Thus, as the BB4 molecules are larger than the BB7 molecules (Fig. 5), the increase in temperature facilitates the desorption of this dye from the solid to the medium.

For DB22 dye, the decrease in membrane adsorption potential with increasing temperature can be associated with two factors. First, the ascending temperature increases the dye molecules' oscillatory energy, hampering the adsorbent/adsorbate interactions [29]. Second, given the medium's acidity, the temperature increase can lead to acid hydrolysis at the membrane surface [30]. In this process, the CN groups of the membrane are protonated, culminating in the material's electronegativity reduction. As discussed earlier, at pH 2, the oxygenated anions of the dye are also protonated [31]. Thus, there is an increase in electrostatic repulsive forces between adsorbent/adsorbate with increasing temperature.

Thus, the optimized temperatures are 25 °C for the DB22 dye and 35 °C for the BB7 and BB4 dyes.

3.3. Adsorption kinetics

The adsorption kinetics of the three dyes was studied under the optimized conditions of each contaminant, varying the initial concentration of BB7, BB4 and DB22 (50–400 $mg{\cdot}L^{-1}$) for 12 h. Pseudo-first order [32], pseudo-second order [33] and intraparticle diffusion [34] kinetic models were fitted to the adsorption curves in linear and non-linear forms and calculations were performed for average relative error (ARE). Values calculated using linearized kinetic models were selected because, they have lower ARE. Therefore, the graphs for the best linear fits of each contaminant and the calculated parameters of the models are presented in Fig. S3 and Table 2, respectively. The criterion to determine the best model involved the highest value of R^2 and the lowest variance between the calculated qe and the experimental qe.

The results indicated the intraparticle diffusion model fit the experimental data for three dyes, with R^2 values ranging from 0.96 to 0.98, 0.92–0.97 and 0.92–0.98 for the dyes BB7, BB4 and DB22, respectively. This model infers that in addition to adsorption, the interactive adsorbent/adsorbate system occurs through mass transfer. The contaminant diffuses from an external layer, the internal structure of the material [35], corroborating the characterizations carried out in hPAN@GO-SF (Table 1), which showed that the membrane is a porous material (89.55 % porosity) with asymmetric and thickened finger-like sublayer.

Regarding the other models, BB7 and DB22 data were better adjusted to the pseudo-first order kinetic model, with calculated qe similar to the experimental one and R^2 values >0.90. In comparison, the pseudo-second-order kinetic model fitted better the BB4 adsorption data. These results indicate that the occupancy rate of the hPAN@GO-SF surface interaction sites by the BB7 and DB22 dyes is proportional to the amount of unoccupied centers on the membrane, while for the BB4

Table 2
Kinetic models parameters of the adsorption of dyes on the hPAN@GO-SF membrane.

		BB7 (mg·L^{-1})				
		50	100	200	300	400
Experimental qe		99.65	205.38	339.17	442.82	635.96
Pseudo-first order	k_1 (min^{-1})	0.0041	0.0021	0.0037	0.0037	0.0028
	q_e (mg·g^{-1})	**97.0287**	**209.2185**	**331.2836**	**551.9503**	**630.8777**
	R^2	**0.9772**	**0.9869**	**0.9586**	**0.9264**	**0.9771**
Pseudo-second order	k_2 (g·mg^{-1}·min^{-1})	1.0417E-05	0.1294	6.2359E-06	1.4715E-06	1.6898E-05
	q_e (mg·g^{-1})	181.8181	3.0166	476.1905	526.3158	625.0000
	R^2	0.7495	0.7822	0.8997	0.3769	0.9567
Intraparticle diffusion	k_{dif} (mg·g^{-1}·min$^{-0,5}$)	**4.2131**	**7.7051**	**14.0270**	**19.9290**	**18.8880**
	R^2	**0.9582**	**0.9454**	**0.9625**	**0.9544**	**0.9788**

		BB4 (mg·L^{-1})				
		50	100	200	300	400
Experimental qe		202.30	388.69	564.68	629.02	766.39
Pseudo-first order	k_1 (min^{-1})	0.0039	0.0029	0.0048	0.0062	0.0023
	q_e (mg·g^{-1})	91.0961	235.9935	315,6458	504.1967	614.7521
	R^2	0.8988	0.9737	0.9752	0.9727	0.9066
Pseudo-second order	k_2 (g·mg^{-1}·min^{-1})	1.40E-04	4.9592E-05	40363E-05	2.4194E-05	1.98E-03
	q_e (mg·g^{-1})	**204.0816**	**370.3704**	**588.2353**	**666.6667**	**769.2307**
	R^2	**0.9958**	**0.9781**	**0.9957**	**0.9334**	**0.9713**
Intraparticle diffusion	k_{dif} (mg·g^{-1}·min$^{-0,5}$)	**4.5964**	**9.6752**	**14.5460**	**19.8640**	**22.2360**
	R^2	**0.9700**	**0.9684**	**0.9241**	**0.9447**	**0.9375**

		DB22 (mg·L^{-1})				
		50	100	200	300	400
Experimental qe		60.34	71.93	88.96	97.74	113.39
Pseudo-first order	k_1 (min^{-1})	0.0034	0.0074	0.0037	0.0037	0.0037
	q_e (mg·g^{-1})	**65.6447**	**75.6983**	**104.5924**	**88.3690**	**121.1435**
	R^2	**0.9814**	**0.9884**	**0.9197**	**0.9733**	**0.9033**
Pseudo-second order	k_2 (g·mg^{-1}·min^{-1})	5.7465E-07	3.1861E-04	9.6181E-06	2.1792E-05	2.1424E-05
	q_e (mg·g^{-1})	434.7826	45.1879	158.7301	140.8450	147.0588
	R^2	< 0.7	0.8495	0.7183	0.9631	0.8546
Intraparticle diffusion	k_{dif} (mg·g^{-1}·min$^{-0,5}$)	**2.5951**	**1.2871**	**3.6970**	**4.0139**	**4.4076**
	R^2	**0.9853**	**0.9202**	**0.9614**	**0.9622**	**0.9765**

Entries in bold refer to the models that best fit the experimental data.

dye this occupancy is proportional to the square of the numbers of unoccupied active sites in the solid [36].

3.4. Effect of NaCl on BB7, BB4 and DB22 adsorption

The recurrent presence of chloride in surface waters highlights the need to study the adsorption equilibrium of new materials in multicomponent systems. Under these conditions, due to competition for substrate interaction centers between the ions and the pollutants present in the medium, there can be significant variation in the adsorption potential of the solid. [37]. This work investigated the removal of BB7, BB4 and DB22 dyes by the adsorption on the membrane in the presence of NaCl salt. The parameters defined for the study were based on the membrane optimization conditions and the concentration of 100 mg·L^{-1} of NaCl (Fig. 3).

As indicated in the analysis (Fig. 3), the presence of salt in the medium resulted in a marked decrease in the adsorption capacity for the cationic dyes and a slight increase in the removal of anionic dye. The qe decreased from 205.4 to 127.5 mg·g^{-1} (38 %) and from 388.7 to 250.9 mg·g^{-1} (35 %) for BB7 and BB4, respectively, and increased from 71.9 to 82.8 mg·g^{-1} (15 %) for DB22 dye.

For cationic dyes, these results indicate competition for the centers of membrane interaction between contaminant molecules and salt ions in the medium [18]. The 38 % and 35 % decrease in adsorbent/adsorbate interactions between hPAN@GO-SF and BB7 and BB4 correspond to electrostatic interactions, ion exchange and hydrogen bonds. This suggests that for these systems >60 % of the interactions are attributed to

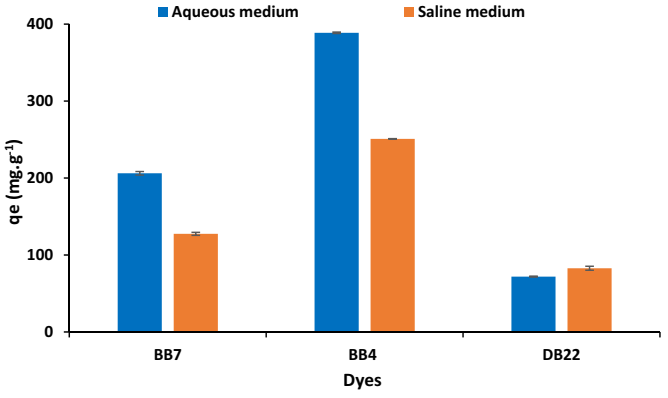

Fig. 3. NaCl effect on the adsorption of BB7, BB4 and DB22 dyes on hPAN@GO-SF membranes. Contact time: 12 h, nanomaterial content: 6 % for BB7 and DB22 and 2 % for BB4, membrane mass: 0.0025 g for BB7 and DB22 and 0.001 g for BB4, initial dye concentration 100 mg·L^{-1}, pH 6 for BB7 and BB4 and pH 2 for DB22, and temperature of 25 °C for DB22 and 35 °C for BB7 and BB4.

π-π and hydrophobic interactions. A like result was observed by Silva et al. [18] when evaluating the effect of saline medium on the adsorption of BB7 complex dye in nanocellulose/GO nanocomposite.

The slight increase in the adsorption capacity of DB22 by

hPAN@GO-SF in a saline medium indicates that the adsorbent/adsorbate interactions are enhanced under this condition. The surplus of Na^+ cations in the solution could induce the covering of the membrane surface through electrostatic interactions with COO^-, making the membrane less electronically rich and more accessible to interact with the negatively charged DB22 dye. Similar results were obtained by Quezada et al. [38] when evaluating the adsorption of an anionic polyelectrolyte on quartz surface in saline medium. According to the authors, the Na^+ cations protected the COO^- groups of the polyelectrolyte and adhered to the solid surface. In turn, these effects provided greater proximity between the materials, favoring interactions by cationic bridge and hydrogen bonds between the polyelectrolyte and quartz [38].

To interpret how the presence of NaCl affects the adsorption equilibrium of the membrane for the dyes, the adsorption isotherm study of the contaminants in saline medium was performed. The Langmuir [39], Freundlich [40], Temkin [41] and Henry [42] isothermal models were fitted to the adsorption data in linear and non-linear forms and calculations were conducted referring to the average relative error (ARE). The values calculated by the linearized isothermal models were selected, since they showed lower ARE. Therefore, the fit of the linearized models to the empirical data and the calculated values for each isotherm are presented in Fig. S4 and Table 3, respectively. The criterion for determining the best model involved a higher value of R^2.

The results revealed that the Temkin model offered a better fit to the empirical data of the BB7 and BB4 dyes, with R^2 of 0.9287 and 0.9296, respectively, and the Henry model was the best adjusted to DB22 data, with R^2 of 0.9057. The Temkin isotherm postulates that adsorbent/adsorbate interactions resulting from the coverage of the solid by the contaminant molecules linearly reduce the heat of adsorption of the interactive process. Thus, the adsorptive process is expressed by a binding energies regular distribution and when maximum, the system saturation is reached [43].

Regarding the Henry model, at low concentrations of adsorbate it expresses that the adsorbent/adsorbate interactions are reduced due to the high affinity of the solute to the solvent, and when at high concentrations, this model fits the Langmuir isotherm [44]. The Langmuir isotherm adopts that the adsorbent/adsorbate interactions are independent of the surface area of the solid, restricting themselves to occur at interactions centers on the adsorbent, and that the maximum saturation occurs when a monomolecular layer of the adsorbate completely covers the surface of the solid [45]. Thus, DB22 dye, when at low concentration in the medium, has a higher affinity with the solvent than to the hPAN@GO-SF membrane. While at high concentrations, possibly due to the size of the contaminant molecule and its affinity for the medium, only a saturated monolayer of the DB22 dye is formed on the membrane.

Table 3
Isothermal adsorption models parameters of the adsorption of dyes on hPAN@GO-SF membrane.

Isothermal models / q_{max} ($mg \cdot g^{-1}$)	BB7 799.74	BB4 1035.36	DB22 147.77
Langmuir			
K_L ($L \cdot mg^{-1}$)	0.0044	0.001	0.0601
q_m ($mg \cdot g^{-1}$)	500.0000	2500.0000	125.0000
R^2	0.8763	0.8363	0.7125
Freundlich			
K_F ($mg^{1-1/n} \cdot g^{-1} \cdot L^{1/n}$)	3.1406	5.2709	32.629
n	0.9596	0.8801	4.3744
R^2	0.8509	0.9048	0.8939
Temkin			
K_T ($L \cdot mg^{-1}$)	**0.0461**	**0.0335**	0.6009
b (kJ/mol)	**7.8484**	**7.168**	104.4155
R^2	**0.9287**	**0.9296**	0.8244
Henry			
K_{HE} = 2.9454	2.5216	2.0998	**0.1378**
R^2 = 0.8399	0.7402	0.9001	**0.9057**

Entries in bold refer to the models that best fit the experimental data.

3.5. Reuse tests

Linked to the reuse of the solid and the operational cost of the process, the replicability of new materials in further adsorption assays without loss of efficiency is an important parameter to be evaluated [46]. Thus, reuse tests were carried out in five consecutive cycles with hPAN@GO-SF membranes, using acidic (pH 2) and basic (pH 12) solutions and organic solvents, acetone and ethyl alcohol, as eluents in the desorption step. The general results of the adsorption of BB7, BB4 and DB22 dyes in consecutive cycles for the different eluent solvents can be seen in Fig. S5 and Fig. 4 summarizes the best results for the three contaminants in the assays.

In the adsorption assays, the maximum adsorption capacity of the cationic dyes was reached at pH 6, and of the anionic dye at pH 2, which leads us to believe that contaminating molecules adhered to the material can be easily removed in acidic and basic solutions, respectively [47]. As expected, the best membrane reuse efficiency for the cationic dyes was achieved using an acidic medium as eluent solvent, while for the anionic dye, this profile was reached using basic conditions. The reason is that in an acidic solution, the protonation of the nitrogen and oxygen groups of the membrane due to the excess of protons on the surface of the material results in electrostatic repulsion between the molecules of the cationic dye and the adsorbent [48], facilitating desorption. In the other case, excess OH^- ions deprotonate the oxygenated groups of the anionic dye and the functional groups of hPAN@GO-SF, increasing the adsorbent/adsorbate repulsive forces [49].

For BB7 (Fig. 4), the hPAN@GO-SF membrane maintained its dye uptake efficiency at 100 % even after five cycles of reuse. Regarding BB4 (Fig. 4), the membrane efficiency was maintained at 100 % until the 4th cycle of solid reuse. In the fifth test, the material's performance dropped 16 % from the previous cycle. Even with a small loss of adsorption capacity, the membrane removal efficiency of 74 % was higher compared to other materials in the literature used in only one adsorption cycle [50]. For DB22 (Fig. 4), hPAN@GO-SF showed 100 % efficiency in up to 3 reuse cycles, showing a 53 % drop in the fourth test and another 24 %

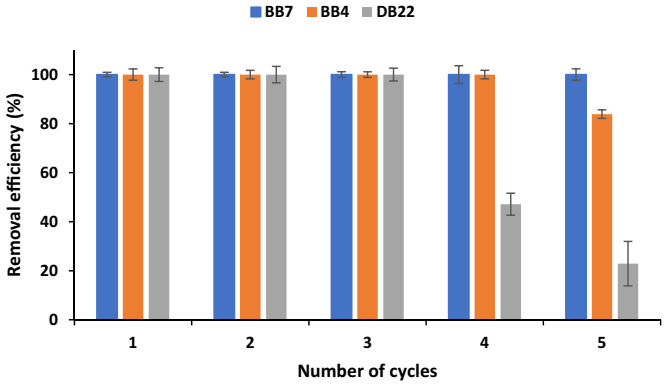

Fig. 4. BB7, BB4 and DB22 reuse assays. Adsorption test: Contact time: 12 h, nanomaterial content in membrane: 6 % for BB7 and DB22 and 2 % for BB4, membrane mass: 0.0025 g for BB7 and DB22 and 0,001 g for BB4, 100 $mg \cdot L^{-1}$ of dyes initial concentration, pH 6 for BB7 and BB4 and pH 2 for DB22, 35 °C for BB7 and BB4, and at room temperature for DB22. Desorption test: Contact time: 12 h, nanomaterial content in membrane: 6 % for BB7 and DB22 and 2 % for BB4, membrane mass: 0.0025 g for BB7 and DB22 and 0,001 g for BB4, 35 °C for BB7 and BB4, and at room temperature for DB22. For the desorption tests the eluent solvent was the acid solution for BB4 and BB7 and basic solution for DB22.

drop in the last cycle. The decrease in membrane removal efficiency for the anionic dye, may be associated with the adsorbent/adsorbate interaction strength. In addition to electrostatic interactions, ion exchange is commonly present in interactions between oppositely charged objects [18], this mechanism raises the enthalpy of binding [51], increasing the energy required to segregate the systems, which culminates in reduced efficiency of the material recycling.

3.6. Adsorption mechanism based on DFT study and FT-IR, XPS and SEM analyses

3.6.1. DFT study

The dye molecules' formulations were optimized using the functional hybrid B3LYP, and two sets of 6-31G bases were compared to verify which one achieved the lowest molecule energy (more stable structure) for each dye. According to Fig. S6, for BB7 and BB4, 6-31G++(d,p) obtained slightly lower energies than 6-31G(d,p), being used to perform the molecular orbital (MO) calculations. For DB22, 6-31G(d,p) was the base set applied to the MO simulations because convergence criteria were not met using 6-31G++(d,p) applied to (MO) calculations.

The optimized geometries are shown in Fig. 5, where the largest dimension of BB7, BB4 and DB22 molecules is 16.1 Å, 18.3 Å and 36.1 Å, respectively. Fig. 5a shows BB7 as a triarylmethane dye with a naphthylamine group. The structure has the triarylmethane rings twisted together due to repulsion forces, giving the molecule a non-planar geometry. BB4 (Fig. 5b) presents a planar conformation with a double azo group (disazo dye) connecting the methyl-benzene-diamine groups and the central toluene group. DB22 (Fig. 5c), in turn, is a sulfonated azo dye that has the flat shape and length characteristic of direct dyes that maximizes van der Waals interactions and dipole hydrogen bonds to cellulose fibers [52].

The three molecules' electrostatic potential (ESP) map is shown in Fig. 5, where the blue color represents positively charged areas, and the red represents the negative regions. Clark et al. [53] mention that the positive charge of cationic dyes can be located in ammonium groups, or it can be arranged as a delocalized charge on the dye cation as found in triarylmethanes, which corroborates the simulation results of BB7 (Fig. 5a) and BB4 (Fig. 5b). For DB22 (Fig. 5c), the negative charge is concentrated around the sulfonated groups. The other regions are at most uncharged, like the extremities of the molecule. The dipole moment of each dye is 5.5, 2.2 and 43.4 Debye, for BB4, BB7, and DB22, respectively.

Fig. 6 shows a rendering of the HOMO and LUMO orbitals of BB7, BB4 and DB22 molecules. HOMO and LUMO show the regions of a molecule that can donor or receive electrons, respectively [54]. HOMO and LUMO are the principal orbitals in a chemical reaction [55]. The HOMO energy is immediately associated with the ionization capacity and the LUMO energy to the electron affinity [56]. Thus, they indicate the reactivity/stability of the structures and determine how the molecule interacts with other species, which is relevant information to describe adsorption mechanisms.

For BB7 (Fig. 6a), HOMO is more concentrated in the naphthylamine group and in one of the arylamine groups. The LUMO density occurs over the three arylamine structures, where electrophilic interactions with the adsorbent occur. In the BB4 molecule (Fig. 6b), the HOMO and LUMO densities are distributed throughout the molecule, indicating that any region can accept and donate electrons, being prone to both electrophilic and nucleophilic interactions with the adsorbent functional groups. In DB22, (Fig. 6c) the HOMO energy density is homogeneously dispersed in all aromatic rings, and LUMO is intensified in the central rings of the molecule. And the HOMO and LUMO orbitals do not present electrical density in the $–SO_3$ group, as also found by Nemr et al. [57]. Comparing the energy gap values of BB4, BB7 and DB22, 3.1, 2.5, and 2.49 eV, respectively, the most stable (less reactive) compound is BB4, which has the greater energy gap. The larger the boundary orbitals, the more energetically unfavorable the energy gap is in adding an electron to the high-lying LUMO and remove electrons from the low-lying HOMO [58]. BB7 and DB22 have similar boundary orbital energy gaps.

Other quantum chemical parameters based on the HOMO and LUMO energies Eqs. (S3)-(S5) are presented in Table 4, such as chemical potential (μ), electron escaping tendency; global chemical hardness (η), resistance to change in electronic density; electrophilicity index (ω), electron-accepting ability [59–61]. Comparing the values of μ, η, and ω for the dyes, BB7 showed the highest chemical potential (μ = 4.3 eV), which means a greater tendency to lose electrons, followed by BB4 (μ = 3.8 eV) and DB22 (μ = 3.8 eV). BB4 is the hardest molecule (η = 1.6 eV), meaning it is more resistant to change in its electronic density, which agrees with the energy gap conclusion that BB4 is the most stable molecule among the three dyes. The ω = 7.5 eV of BB7 confirmed the greater electrophilic nature of this dye. The intermediary electrophilicity index of DB22 (5.6 eV) suggests that, despite the negative charge of the compound in aqueous solution, this dye has a more remarkable ability to accept electrons than BB4, a cationic species. This may be related to the high chemical hardness of BB4, which makes significant changes in charge density.

These results suggest that the adsorption potential of the hPAN@GO-SF membrane by π-π interactions should be higher for DB22 dye, the most reactive molecule, than for BB7 and BB4 dyes. However, the adsorption assays indicated that BB4 was the dye best removed by the membrane (2.5 $mmol \cdot g^{-1}$), followed by BB7 (1.7 $mmol \cdot g^{-1}$) and DB22 (0.2 $mmol \cdot g^{-1}$) (Table 4). These divergences between the calculated data and results obtained in the adsorption experiments suggest that besides π-stacking [62], other interactions may be predominant in removing the dyes by hPAN@GO-SF.

The adsorption tests indicated the presence of electrostatic interactions and hydrogen bonds in removing dyes through the membrane. In agreement, the tests in saline media, when demonstrating that the presence of ions influenced the adsorbent/adsorbate interactions, confirmed the presence of electrostatic interactions and hydrogen bonding between the membrane and dyes, which were estimated at 38 %, 35 %, and 15 % for BB7, BB4 and DB22 dyes (Fig. 3), respectively. Regarding electrostatic interactions, the hPAN@GO-SF membrane, due to its electronegative surface charge, has a greater affinity for cationic dyes and, corroborating the DFT study, the BB7 molecules, having cations homogeneously distributed along their structure, present a higher electrostatic potential than BB4 molecules, with have localized cations. Regarding hydrogen bonds, as the contaminant molecules BB7 and BB4 have NH and OH groups in their structure, they can interact the membrane carboxyl groups [63]. Because it is proximity-based binding, this type of interaction is difficult for DB22 and BB7 molecules. For the anionic dye, the electrostatic repulsions hinder the adsorbent/adsorbate proximity. For the cationic BB7 dye, the four aromatic rings attached to the nitrogen groups in the structure cause a steric hindrance to form the OH/NH groups to the COO^- of hPAN@GO-SF. Thus, hydrogen bonds are more effective between the BB4 dye molecules and the material.

Regarding π-stacking, the BB7 dye has a nucleus with 4 aromatic rings (triarylmethane group), presenting a large rigid three-dimensional structure, making it challenging to pair the molecule of contaminant and the benzyl groups of the membrane [64]. On the other hand, the BB4 and DB22 molecules, because they have a smaller nucleus with a linear structure, have greater mobility, enabling different conformations between adsorbent/adsorbate, and consequently facilitating the π-π interactions.

The discussions held above indicated that BB4 interacts with hPAN@GO-SF through H-bonding, electrostatic and π-π interactions, while the BB7 and DB22 dyes, do so through electrostatic and π-π interactions. Which denotes the best membrane removal potential for BB4, followed by BB7 and DB22. For DB22, the adsorbent/adsorbate electrostatic repulsions indicative a decrease in the membrane adsorption potential for the contaminant. The three-dimensional structure of the compound and the large molecule size may contribute to the steric impediment of the compound on the hPAN@GO-SF surface [65].

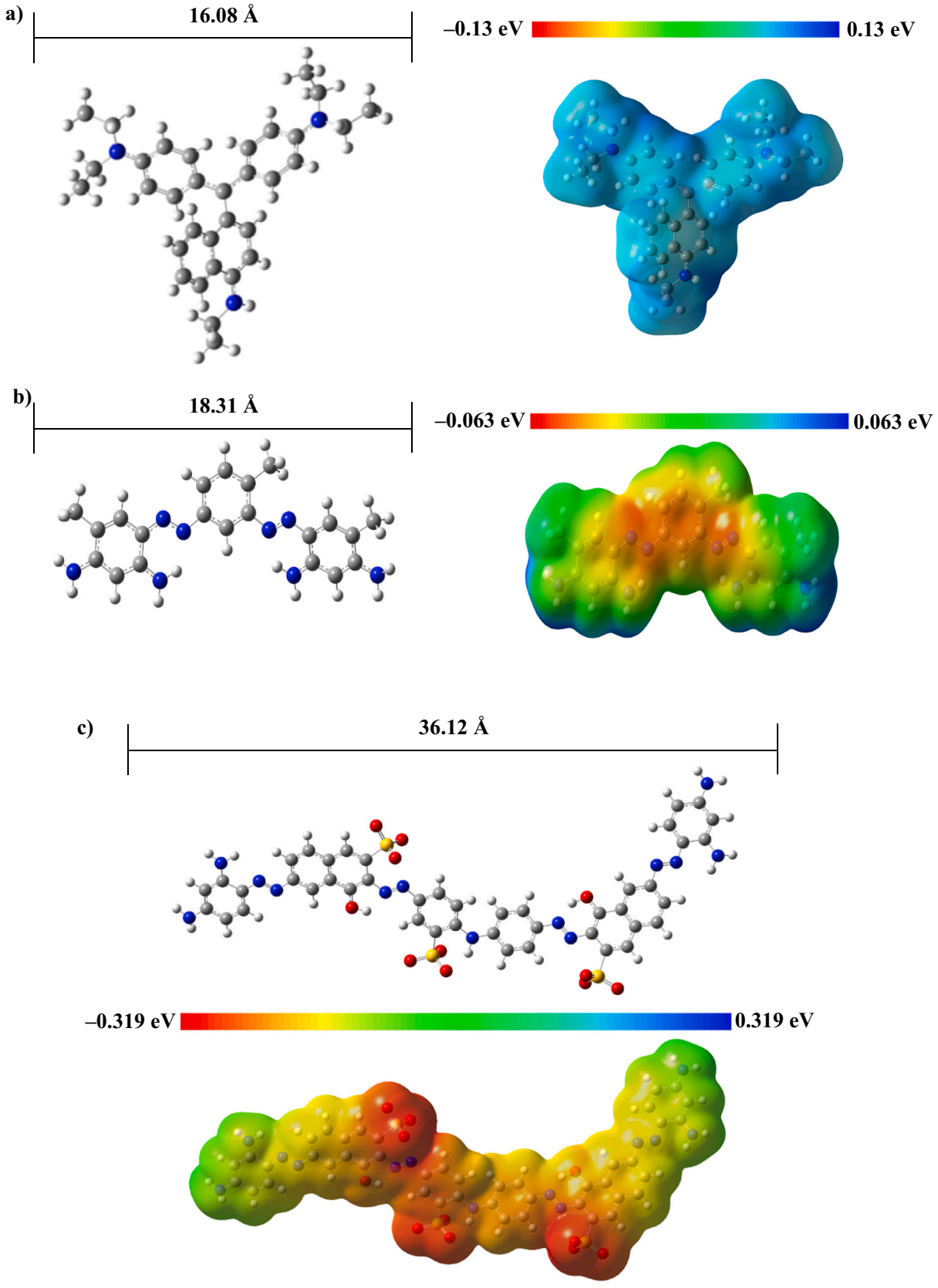

Fig. 5. Optimized structure and ESP map of a) BB7, b) BB4 and c) DB22. (blue color: positively charged zones; red color: negative zones). (For interpretation of the references to color in this figure legend, the reader is referred to the web version of this article.)

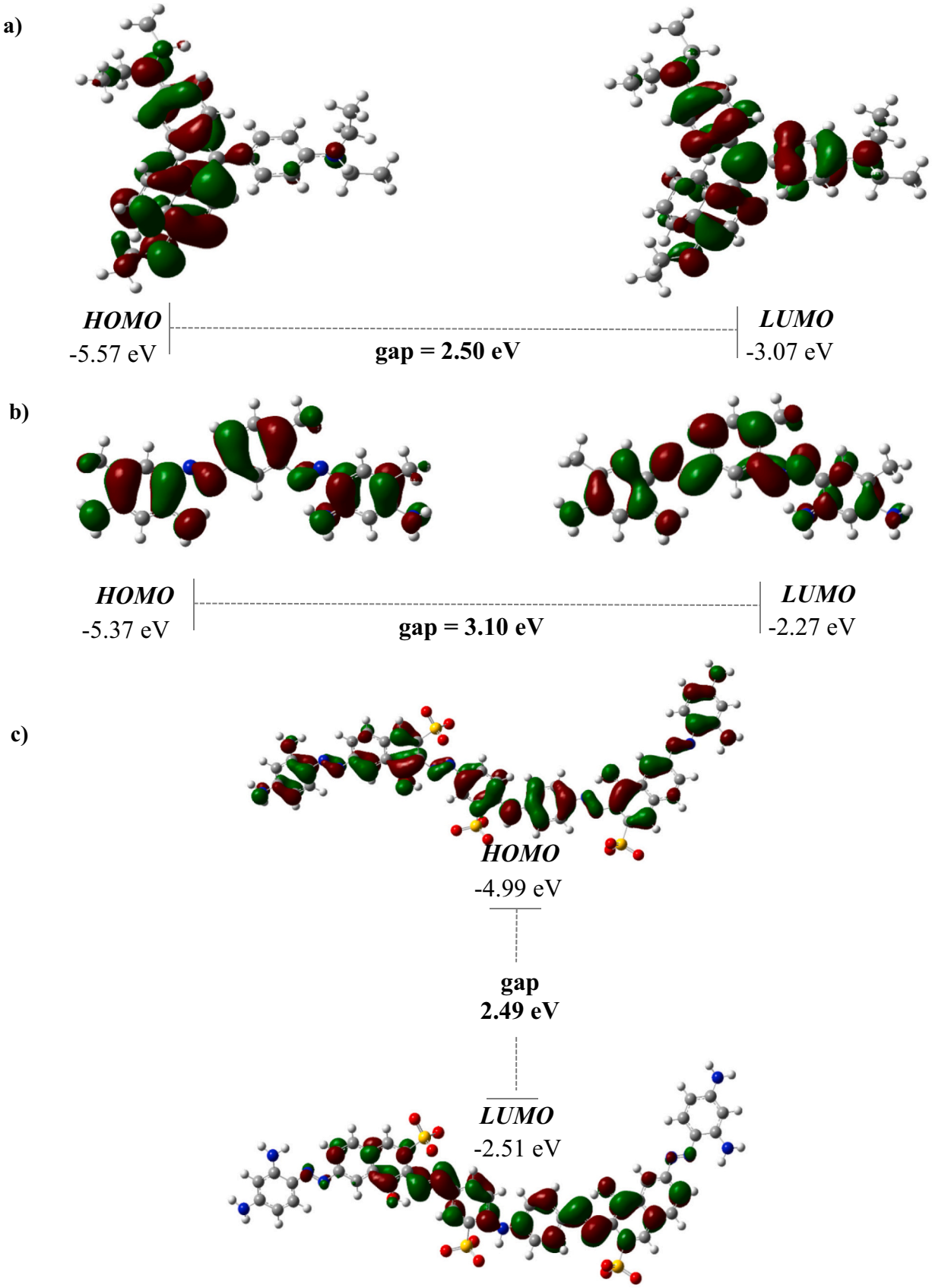

Fig. 6. HOMO and LUMO orbitals of a) BB7, b) BB4 and c) DB22. Positive (red) and negative (green) phase distributions in the molecular orbital wave function. (For interpretation of the references to color in this figure legend, the reader is referred to the web version of this article.)

Table 4
Quantum chemical parameters calculated for the dyes BB4, BB7 and DB22.

Molecular Chemical Descriptors	BB7	BB4	DB22
Experimental qe (mmol·g^{-1})	1.7	2.5	0.2
HOMO energy (EH, eV)	−5.57	−5.37	−4.99
LUMO energy (EL, eV)	−3.07	−2.27	−2.51
Energy gap (ΔH-L, eV)	2.50	3.10	2.49
Chemical Potential (μ, eV)	4.32	3.82	3.75
Chemical hardness (η, eV)	1.25	1.55	1.24
Electrophilicity index (ω, eV)	7.47	4.70	5.65

3.6.2. FT-IR, XPS and SEM post-adsorption processing analyses

To further explore the possible mechanisms of dye interactions with hPAN@GO-SF membranes, in addition to the DFT study, FTIR, XPS and SEM analyses were carried out on post-adsorption materials.

FTIR analysis was employed to delineate variations in membrane functional groups according to dye adsorption onto the structure (Fig. 7). Analyzing the hPAN@GO-SF FT-IR spectrum (black line, Fig. 7) it was possible to denote functional groups characteristic of the partially hydrolyzed polymer and GO-SF. The broad signal in the region of 3436 cm^{-1}, the small bands at 2931 and 2864 cm^{-1} and the sharp vibration at 2240 cm^{-1} are associated to OH stretching, the symmetrical and asymmetrical bending of CH units and nitriles (C≡N), respectively [10]. The bands centered at 1696, 1573, 1457, 1398, 1222 and 1074 cm^{-1} are assigned to C═C, NH, CH_2 bonds, OH inflections, CO inflections and COC elongations, respectively [66]. These conformations were also observed in the membrane spectra with the adsorbed dyes BB7 (red line, Fig. 7), BB4 (blue line, Fig. 7) and DB22 (pink line, Fig. 7), except for some variations, such as displacement, convalescence and appearance of bands. These changes indicate the existence of interactions between adsorbent/adsorbate.

The bands associated to OH (3436 cm^{-1}) and NH (1573 cm^{-1}) in the hPAN@GO-SF spectrum blue-shifted to 3428, 3424 and 3420 cm^{-1} and 1568, 1567 and 1587 cm^{-1} in the membrane spectra with BB7, BB4 and DB22 adsorbed, respectively (Fig. 7). This indicate the existence of adsorbent/adsorbate H-bonding and variations in the counter-ions, related to the oxygenated groups of membrane and DB22 and the nitrogenous groups of BB7 and BB4 [67]. Furthermore, the hPAN@-GOSF band shifted at 1696 cm^{-1} to 1646, 1691 and 1684 cm^{-1} for BB7, BB4 and DB22 dyes, respectively (Fig. 7), suggesting the attendance of π-stacking between adsorbent/adsorbate [68].

XPS analysis was used to evaluate how adsorption of the dyes influenced the elemental arrangement of the membranes (Table 5), as well as to obtain information on the chemical bonds between the material and the dyes (Fig. 8). The XPS spectrum (Table 5) indicated the attendance of elements C, O, N, Na and Cl in 75.6 %, 11.0 %, 12.6 %, 0.2 % and 0.6 % for hPAN@GO-SF 2 % and 76.4 %, 10.3 %, 12.5 %, 0.1 % and 0.7 % for the membrane incorporated with 6 % of GO-SF. The proportion of these elements in membranes with loaded dyes varied, indicating the presence of contaminants in the membrane. Regarding the membrane adsorbed BB4 (Table 5), the contents of C, N, O, Cl and Na were 73.5 %, 16.0 %, 10.0 %, 0.3 % and 0.2 %, respectively. The rise in N was expected since the dye is endowed with nitrogen groups in its structure. For the membrane incorporated with 6 % of GO-SF adsorbed BB7 (Table 5), the contents were 72.1 %, 17.0 %, 17.0 %, 0.6 % and 0.1 % were found for the elements described above, respectively, indicating that, like BB4, BB7 is endowed with N. The hPAN@GO-SF 6 % loaded with DB22 (Table 5), showed 71.0 %, 14.1 %, 12.3 %, 2.4 %, 0.1 % and 0.1 % for C, N, O, S, Na and Cl, respectively. The enhancement of O and N, and advent of the S element, indicated the presence of DB22 dye in the material. Furthermore, a decrease in the Cl content of the membrane with anionic dye, indicates that there was anion exchange between the oxygen groups of the dye and the Cl^- in the SF [67], attesting to the adsorption of DB22 to the membrane.

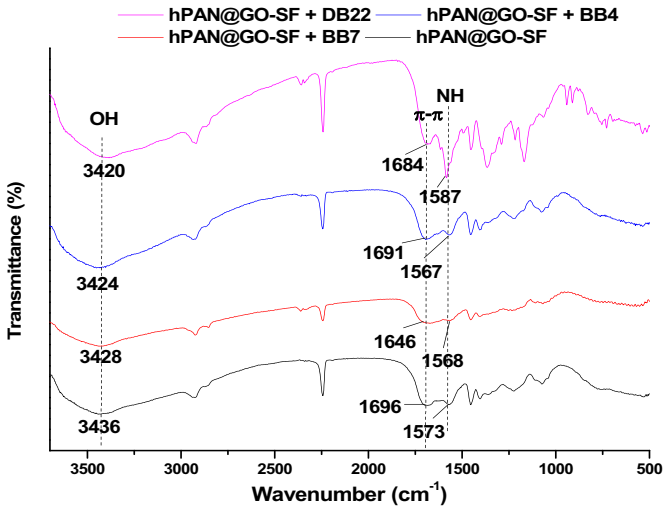

Fig. 7. Pristine membrane (black), hPAN@GO-SF 6 % + BB7 (red), hPAN@GO-SF 2 % + BB4 (blue) and hPAN@GO-SF 6 % + DB22 (pink) FTIR spectrum. (For interpretation of the references to color in this figure legend, the reader is referred to the web version of this article.)

Deconvolution of the high resolution C1s spectra of membranes with loaded dyes (Fig. 8a, c, e) indicated changes in peak intensities, as well as variations in binding energy, indicating possible adsorbent/adsorbate interactions. Changes in binding energy related to the ethylene groups, from 284.2 eV (Table 1) to 284.0, 284.3 and 284.6 eV for the DB22, BB4 and BB7, respectively, indicate the attendance of π-π interactions of contaminating phenyl groups and the membrane [68]. Changes in signals related to CO/CN from 285.1 eV (Table 1) to 285.3, 285.7 and 285.9 eV for DB22, BB7, and BB4, respectively, suggest hydrogen bonds between the dyes and hPAN@GO-SF [69]. Variations in the C═O binding energy from 287.2 eV (Table 1) to 287.6, 287.3 and 287.5 eV for BB7, BB4 and DB22, respectively, indicate that carbonyl functional groups acted as hydrogen bond acceptor [70]. The N1s high-resolution XPS spectrum of membrane after adsorption (Fig. 8b, d, f) showed shifts in binding energies and peak intensities variation for each dye, indicating the participation of N as an electron acceptor in hydrogen bonds [18]. The peaks concerning to the CN/C ≡ N and C═N/NCO groups shifted from 399.2 and 399.9 eV (Table 1) to 399.7 and 400.0 eV for BB7, 399.1 and 400.4 eV for BB4 and 399.1 and 400.1 eV for DB22, respectively [71]. These results indicate that nitrogen functions have a significant impact on the adsorption process, due to H-bonding.

SEM analysis was also performed to investigate the morphology of the membranes after adsorption (Fig. 9). The images obtained indicated the attendance of dyes on the membrane surface, highlighting the contaminants as light gray particles on the dark gray material. Furthermore, by the technique it is clear that the mass of the adsorbed BB7 and BB4 dyes is greater than for DB22 dye, since the images show higher concentration of dye per membrane area for the cationic dye crystal. These results corroborate the tests performed, which showed that the hPAN@GO-SF membrane has an average adsorption capacity of 1143.1, 873.7 and 204.9 mg·g^{-1} for BB4, BB7 and DB22, respectively.

Table 5
Data obtained for membranes by XPS survey.

Material	Content					
	C(%)	O(%)	N(%)	Na(%)	Cl(%)	S(%)
hPAN@GO-SF 2 %	75.6	11.0	12.6	0.2	0.6	–
hPAN@GO-SF 2 % + BB4	73.5	10.0	16.0	0.2	0.3	–
hPAN@GO-SF 6 %	76.4	10.3	12.5	0.1	0.7	–
hPAN@GO-SF 6 % + BB7	72.1	10.2	17.0	0.1	0.6	–
hPAN@GO-SF 6 % + DB22	71.0	12.3	14.1	0.1	0.1	2.4

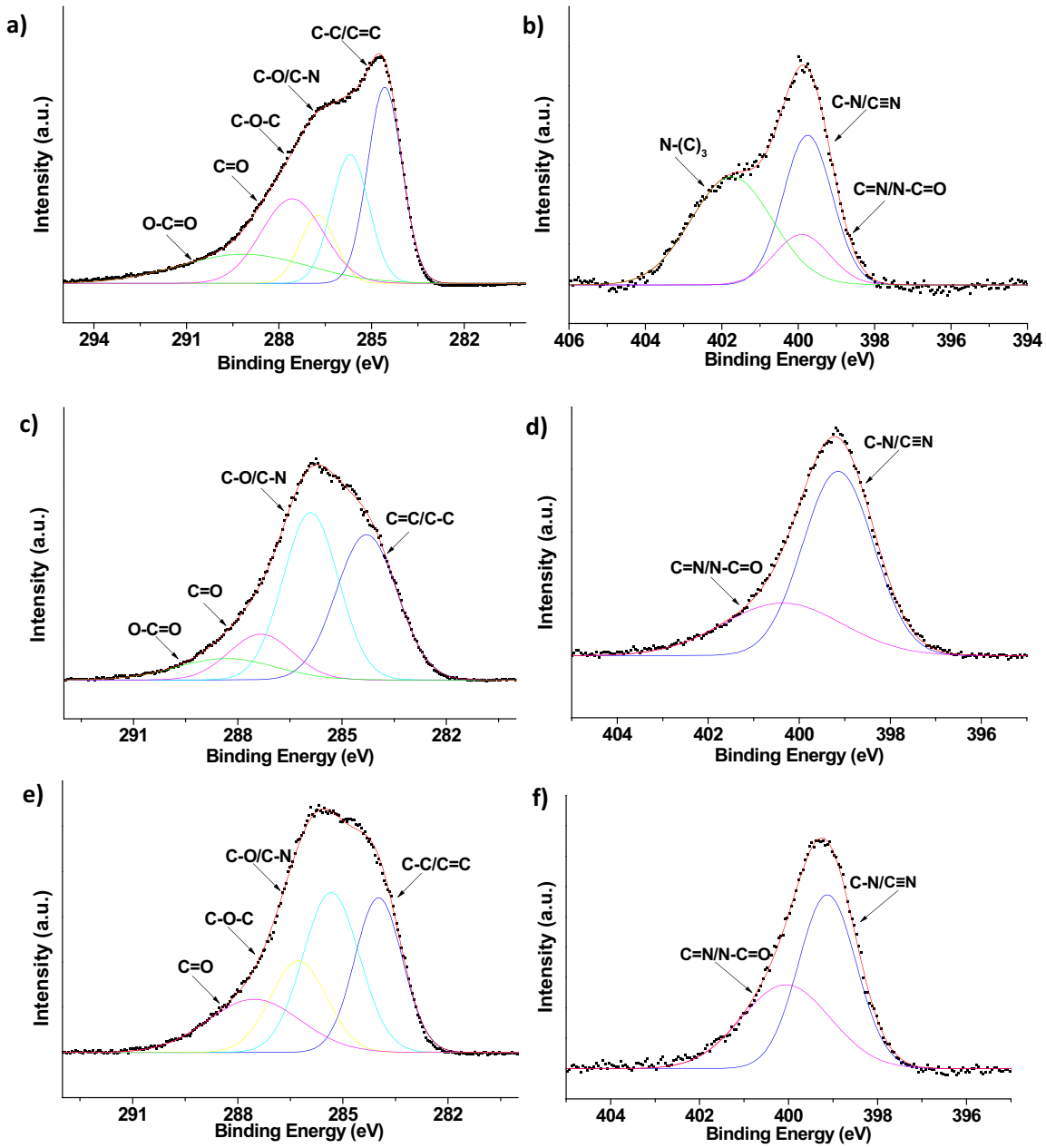

Fig. 8. a) High-resolution C1s XPS spectra of a) Membrane adsorbed BB7, c) Membrane adsorbed BB4 and e) Membrane adsorbed DB22. High-resolution N1s XPS spectra of b) Membrane adsorbed BB7, d) Membrane adsorbed BB4 and e) Membrane adsorbed DB22.

3.6.3. hPAN@GO-SF adsorption mechanism

The hPAN@GO-SF membrane, when used in singular systems for the removal of BB7, BB4 and DB22 dyes showed expressive adsorption capacity due to adsorbent/adsorbent interactions. The optimization study suggested that electrostatic and π-π interactions were critical in the adsorption of the dye by the membrane. Corroborating these perspectives, the assay in saline medium revealed that 38, 35 and 15 % of the interactive processes between hPAN@GO-SF and the dyes are by electrostatic interactions and H-bonding [72]. DFT study showed that π-π govern the process, and are most expressive for the dye DB22. Post-adsorption characterizations confirmed that ion exchange, H-bonding, π-stacking and electrostatic interactions rule adsorption mechanisms, with electrostatic and π- π interactions being the main ones (Fig. 10).

The maximum qe of hPAN@GO-SF for the BB4, BB7 and DB22 dyes of 1143.1, 873.7 and 204.9 $mg{\cdot}g^{-1}$ indicated the remarkable removal potential of the membranes, which obtained values higher than most tridimensional materials reported in the literature (Table 6). In general, for the materials used in the literature (Table 6), the new membranes presented greater mass, and even in these circumstances, hPAN@GO-SF stood out from the others.

4. Conclusions

In this study, GO-based polymeric membranes functionalized with SF dye were applied to treat complex dyes, such as the cationic dyes BB7 and BB4 and the anionic dye DB22 from water. The membrane, hPAN@GO-SF, was used in batch assays because previous studies showed that its selectivity varied with permeate flux and due to facile removal of the material post-process from the aqueous solution. The optimized experimental conditions indicated that the medium pH and temperature are important parameters for the dye removal by the membranes. The maximum adsorption potential of 1143.1 $mg{\cdot}g^{-1}$,

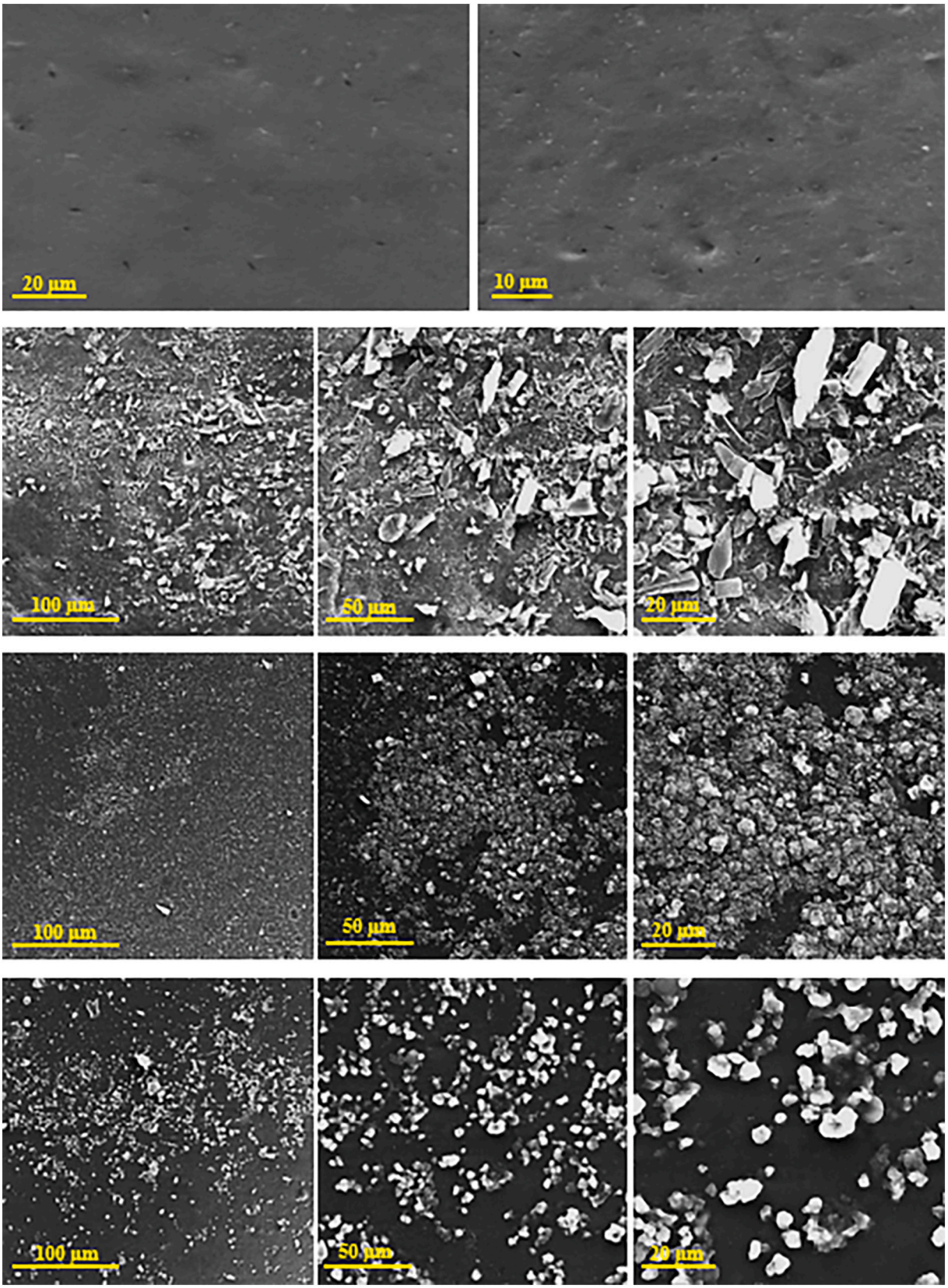

Fig. 9. SEM images of the surfaces a) Membrane endowed with 2 % of GO-SF b) Membrane endowed with 6 % of GO-SF, c1–3) hPAN@GO-SF 6 % + BB7, d1–3) hPAN@GO 2 % + BB4 and e1–3) PAN/GO-SF 6 % + DB22.

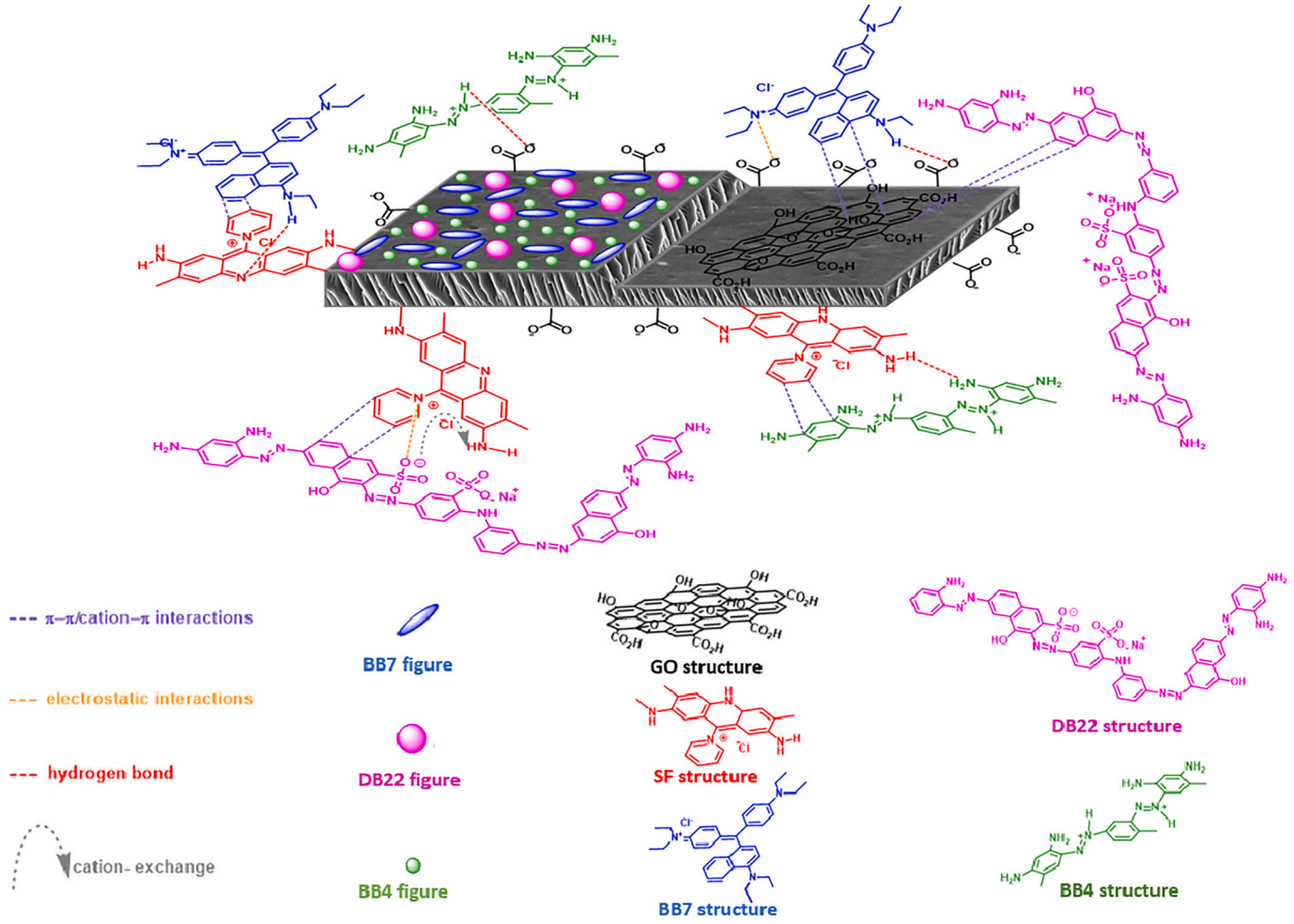

Fig. 10. Adsorption mechanisms of BB7, BB4 and DB22 on the hPAN@GO-SF.

Table 6
Comparison between the removal potential of hPAN@GO-SF and other 3D adsorbents.

Adsorbents	Dyes	Morphology	pH	Temperature	q_m (mg·g^{-1})	Ref.
HCP–1	BB7	Microporous polymer	6	25 °C	496.7	[73]
Si–POP–1	BB7	Porous polymer	5–7	25 °C	44.0	[74]
Si–POP–2	BB7	Porous polymer	5–7	25 °C	740.0	[74]
CS/TPP	BB7	Beads	6	25 °C	1410.1	[4]
hPAN@GO-SF	**BB7 + NaCl**	**Membrane**	**6**	**35 °C**	**799.7**	**This work**
hPAN@GO-SF	**BB7**	**Membrane**	**6**	**35 °C**	**873.7**	**This work**
IONs	BB4	Nanosphere	10	55 °C	34.0	[75]
MIONS	BB4	Nanosphere	6.7	55 °C	54.9	[75]
Hen Feather	BB4	Barbs	3	50 °C	240	[76]
hPAN@GO-SF	**BB4 + NaCl**	**Membrane**	**6**	**35 °C**	**1035.4**	**This work**
hPAN@GO-SF	**BB4**	**Membrane**	**6**	**35 °C**	**1143.1**	**This work**
Chitosan	DB22	Beads	5	r.t.	40.0	[77]
Sawdust immobilized in chitosan	DB22	Beads	5	r.t.	50.0	[77]
Ash immobilized in chitosan	DB22	Beads	5	r.t.	51.0	[77]
hPAN@GO-SF	**DB22 + NaCl**	**Membrane**	**2**	**25 °C**	**147.8**	**This work**
hPAN@GO-SF	**DB22**	**Membrane**	**2**	**25 °C**	**204.9**	**This work**

Entries in bold refer to the experimental data obtained in this work.

873.7 mg·g^{-1} and 204.9 mg·g^{-1} for BB4, BB7 and DB22, respectively, were obtained at pH 6 and 35 °C for complex cationic dyes and pH 2 and 25 °C for complex anionic dye.

The adsorption kinetics for the single system indicated that the intraparticle diffusion model fitted the experimental data for the three dyes and the pseudo-first order kinetics fitted the BB7 and DB22 data, while the pseudo-second order kinetics fitted the BB4's data. The tests in saline medium indicated that electrostatic interactions, ion exchange and hydrogen bonds were common to the adsorbent/adsorbate processes and corresponded to 38, 35 and 15 % of the interactive processes between hPAN@GO-SF and the dyes BB7, BB4 and DB22, respectively. Furthermore, studies of the adsorption isotherm for the dyes in saline medium showed that the maximum membrane adsorption capacities for the dyes in the presence of NaCl were 1035, 799 and 148 mg·g^{-1} for BB7, BB4 and DB22, respectively, and indicated that the interactions between the hPAN@GO-SF and the cationic dyes and the anionic dye

could be expressed by the Temkin and Henry isothermal models, respectively.

The DFT study of the contaminants indicated that π-π interactions were expected in the process and that the most reactive dye was DB22, followed by BB7 and BB4, respectively. Experimental adsorption data and FTIR, XPS and SEM analyses performed post-adsorption processing showed that ion exchange, hydrogen bonding, π-π and electrostatic interactions, govern the system. Thus, from the mechanisms linked to the interactive process between the membrane and the dyes, electrostatic and π-π interactions stand out. The material maintained the high removal efficiency even after 3 cycles of reuse, confirmimg the weak bonds of adsorbent/adsorbate polarization. The potential of the membrane for dye removal was attested by other 3D materials, indicating the effectiveness of the new material.

CRediT authorship contribution statement

Tauany de Figueiredo Neves: Methodology, Investigation, Data curation, Formal analysis, Validation, Software, Writing – original draft, Writing – review & editing. **Natália Gabriele Camparotto:** Data curation, Formal analysis, Validation, Software, Writing – review & editing. **Giani de Vargas Brião:** Formal analysis, Validation, Software, Writing – original draft, Writing – review & editing. **Valmor Roberto Mastelaro:** Investigation, Formal analysis, Software, Writing – review & editing. **Renato Falcão Dantas:** Funding acquisition, Resources, Supervision, Writing – review & editing. **Melissa Gurgel Adeodato Vieira:** Investigation, Formal analysis, Writing – review & editing. **Patrícia Prediger:** Funding acquisition, Resources, Project administration, Investigation, Data curation, Formal analysis, Writing – review & editing.

Declaration of competing interest

The authors declare that they have no known competing financial interests or personal relationships that could have appeared to influence the work reported in this paper.

Data availability

Data will be made available on request.

Acknowledgements

The funding acquisition of the research was acquired by Fund for Support to Teaching, Research and Outreach Activities (FAEPEX), Coordination for the Improvement of Higher Education Personnel (CAPES) (Finance Code 001), the São Paulo Research Foundation (FAPESP, n. 2019/25228-0, 2019/07822-2 and 2013/07296-2) and Brazilian National Research Council (CNPq). For the SEM analysis and graphic designers, the authors thankful to Dr. Josiane Vendemiatti and Gustavo Paixão. The molecular simulation was developed with the support of Centro Nacional de Processamento de Alto Desempenho (CENAPAD/SP).

Appendix A. Supplementary data

Supplementary data to this article can be found online at https://doi.org/10.1016/j.jwpe.2022.103248.

References

[1] J.El Gaayda, F.Ezzahra Titchou, R. Oukhrib, I. Karmal, H.Abou Oualid, A. Berisha, H. Zazou, C. Swanson, M. Hamdani, R.Ait Akbour, Removal of cationic dye from coloured water by adsorption onto hematite-humic acid composite: Experimental and theoretical studies, Sep. Purif. Technol. 288 (2022) 120607, https://doi.org/10.1016/J.SEPPUR.2022.120607.

[2] O. Menezes, R. Brito, F. Hallwass, L. Florêncio, M.T. Kato, S. Gavazza, Coupling intermittent micro-aeration to anaerobic digestion improves tetra-azo dye direct black 22 treatment in sequencing batch reactors, Chem. Eng. Res. Des. 146 (2019) 369–378, https://doi.org/10.1016/J.CHERD.2019.04.020.

[3] R. Jamee, R. Siddique, Biodegradation of synthetic dyes of textile effluent by microorganisms: an environmentally and economically sustainable approach, Eur. J. Microbiol. Immunol. (Bp). 9 (2019) 114, https://doi.org/10.1556/1886.2019.00018.

[4] P.M. Silva, N.G. Camparotto, T.F. Neves, K.T.G. Lira, V.R. Mastelaro, C.S.F. Picone, P. Prediger, Effective removal of basic dye onto sustainable chitosan beads : batch and fixed-bed column adsorption, beads stability and mechanism, Sustain. Chem. Pharm. 18 (2020), 100348, https://doi.org/10.1016/j.scp.2020.100348.

[5] S. Celik, N. Duman, F. Sayin, S. Tunali Akar, T. Akar, Microbial cells immobilized on natural biomatrix as a new potential ecofriendly biosorbent for the biotreatment of reactive dye contamination, J. Water Process Eng. 39 (2021), 101731, https://doi.org/10.1016/J.JWPE.2020.101731.

[6] S.P. Ghuge, A.K. Saroha, Catalytic ozonation of dye industry effluent using mesoporous bimetallic ru-Cu/SBA-15 catalyst, Process Saf. Environ. Prot. 118 (2018) 125–132, https://doi.org/10.1016/J.PSEP.2018.06.033.

[7] A.I. Abd-Elhamid, E.A. Kamoun, A.A. El-Shanshory, H.M.A. Soliman, H.F. Aly, Evaluation of graphene oxide-activated carbon as effective composite adsorbent toward the removal of cationic dyes: composite preparation, characterization and adsorption parameters, J. Mol. Liq. 279 (2019) 530–539, https://doi.org/10.1016/J.MOLLIQ.2019.01.162.

[8] J.R. De Andrade, M.F. Oliveira, M.G.C. Da Silva, M.G.A. Vieira, Adsorption of pharmaceuticals from water and wastewater using nonconventional low-cost materials: a review, Ind. Eng. Chem. Res. 57 (2018) 3103–3127, https://doi.org/10.1021/acs.iecr.7b05137.

[9] S. Cinti, F. Arduini, Graphene-based screen-printed electrochemical (bio)sensors and their applications: efforts and criticisms, Biosens. Bioelectron. (2017), https://doi.org/10.1016/j.bios.2016.07.005.

[10] T.F. Neves, N.Barticiotto Dalarme, P.M.M. da Silva, R. Landers, C.Siqueira Franco Picone, P. Prediger, Novel magnetic chitosan/quaternary ammonium salt graphene oxide composite applied to dye removal, J. Environ. Chem. Eng. 8 (2020), https://doi.org/10.1016/j.jece.2020.103820.

[11] Y. He, C. Yi, X. Zhang, W. Zhao, D. Yu, Magnetic graphene oxide: synthesis approaches, physicochemical characteristics, and biomedical applications, TrAC Trends Anal. Chem. 136 (2021), 116191, https://doi.org/10.1016/J.TRAC.2021.116191.

[12] E.F.D. Januário, T.B. Vidovix, R.M. Paixão, L.H.B.R. da Silva, N.C. Homem, R. Bergamasco, A.M.S. Vieira, Advanced graphene oxide-based membranes as a potential alternative for dyes removal: A review, Sci. Total Environ. 789 (2021) 147957, https://doi.org/10.1016/J.SCITOTENV.2021.147957.

[13] J. Zhu, M. Tian, J. Hou, J. Wang, J. Lin, Y. Zhang, J. Liu, B.Van Der Bruggen, Surface zwitterionic functionalized graphene oxide for a novel loose nanofiltration membrane †, 2016, https://doi.org/10.1039/c5ta08024j.

[14] L. Das, P. Das, A. Bhowal, C. Bhattachariee, Synthesis of hybrid hydrogel nanopolymer composite using graphene oxide, chitosan and PVA and its application in waste water treatment, Environ. Technol. Innov. 18 (2020), 100664, https://doi.org/10.1016/J.ETI.2020.100664.

[15] N.G. Camparotto, E.A. Rodrigues, V.R. Mastelaro, R.F. Dantas, P. Prediger, New graphene oxide-safranin modified@polyacrylonitrile membranes for removal of emerging contaminants: The role of chemical and morphological features, Chem. Eng. J. 446 (2022) 137176, https://doi.org/10.1016/J.CEJ.2022.137176.

[16] A. Ghaly, A.S. Mahmoud, A.E. Ghaly, S.L. Brooks, Influence of temperature and pH on the stability and colorimetric measurement of textile dyes, Am. J. Biotechnol. Biochem. 3 (2007) 33–41.

[17] G. Zhang, R. Li, X. Wang, X. Chen, Y. Shen, Y. Fu, The inhibiting water uptake mechanism of main-chain type N-spirocyclic quaternary ammonium ionene blended with polybenzimidazole as anion exchange membrane, Sep. Purif. Technol. 291 (2022), 120950, https://doi.org/10.1016/J.SEPPUR.2022.120950.

[18] P.M.M. da Silva, N.G. Camparotto, T.Figueiredo Neves, V.R. Mastelaro, B. Nunes, C.Siqueira Franco Picone, P. Prediger, Instantaneous adsorption and synergic effect in simultaneous removal of complex dyes through nanocellulose/graphene oxide nanocomposites: Batch, fixed-bed experiments and mechanism, Environ. Nanotechnology, Monit. Manag. 16 (2021), https://doi.org/10.1016/j.enmm.2021.100584.

[19] M. Khansanami, A. Esfandiar, High flux and complete dyes removal from water by reduced graphene oxide laminate on poly vinylidene Fluoride/graphene oxide membranes, Environ. Res. 201 (2021), 111576, https://doi.org/10.1016/J.ENVRES.2021.111576.

[20] G. Zhao, H. Zhu, Cation-π interactions in graphene-containing systems for water treatment and beyond, Adv. Mater. 1905756 (2020) 1–22, https://doi.org/10.1002/adma.201905756.

[21] R. Gusain, N. Kumar, S.S. Ray, Recent advances in carbon nanomaterial-based adsorbents for water purification, Coord. Chem. Rev. 405 (2020), 213111, https://doi.org/10.1016/j.ccr.2019.213111.

[22] H. Mittal, A. Al Alili, P.P. Morajkar, S.M. Alhassan, Graphene oxide crosslinked hydrogel nanocomposites of xanthan gum for the adsorption of crystal violet dye, J. Mol. Liq. 323 (2021), 115034, https://doi.org/10.1016/J.MOLLIQ.2020.115034.

[23] M. Özacar, I.A. Şengil, Adsorption of metal complex dyes from aqueous solutions by pine sawdust, Bioresour. Technol. 96 (2005) 791–795, https://doi.org/10.1016/J.BIORTECH.2004.07.011.

[24] G. Sharma, M. Naushad, A. Kumar, S. Rana, S. Sharma, A. Bhatnagar, F.J. Stadler, A.A. Ghfar, M.R. Khan, Efficient removal of coomassie brilliant blue R-250 dye using starch/poly(alginic acid-cl-acrylamide) nanohydrogel, Process Saf. Environ. Prot. 109 (2017) 301–310, https://doi.org/10.1016/J.PSEP.2017.04.011.

[25] T. de Figueiredo Neves, P. Kushima Assano, L. Rodrigues Sabino, W. Bardelin Nunes, P. Prediger, Influence of adsorbent/adsorbate interactions on the removal of cationic surfactants from water by graphene oxide, water, Air. Soil Pollut. 231 (2020) 1–22, https://doi.org/10.1007/s11270-020-04669-w.
[26] B. Hayati, A. Maleki, F. Najafi, H. Daraei, F. Gharibi, G. McKay, Synthesis and characterization of PAMAM/CNT nanocomposite as a super-capacity adsorbent for heavy metal (Ni2 +, Zn2 +, As3 +, Co2 +) removal from wastewater, J. Mol. Liq. 224 (2016) 1032–1040, https://doi.org/10.1016/J.MOLLIQ.2016.10.053.
[27] A.W. Marczewski, M. Seczkowska, A. Deryło-Marczewska, M. Blachnio, Adsorption equilibrium and kinetics of selected phenoxyacid pesticides on activated carbon: effect of temperature, Adsorption 22 (2016) 777–790, https://doi.org/10.1007/s10450-016-9774-0.
[28] F.A. Taher, F.H. Kamal, N.A. Badawy, A.E. Shrshr, Hierarchical magnetic/chitosan/graphene oxide 3D nanostructure as highly effective adsorbent, Mater. Res. Bull. 97 (2018) 361–368, https://doi.org/10.1016/j.materresbull.2017.09.023.
[29] M.Ángeles Fontecha-Cámara, M.Victoria López-Ramón, Miguel A. Álvarez-Merino, Carlos Moreno-Castilla, Temperature Dependence of Herbicide Adsorption from Aqueous Solutions on Activated Carbon Fiber and Cloth, Langmuir. 22 (2006) 9586–9590, https://doi.org/10.1021/LA061666V.
[30] M. Dörr, Acid hydrolysis, encycl, Astrobiol. (2011) 10, https://doi.org/10.1007/978-3-642-11274-4_21, 10.
[31] A.D. Litmanovich, N. Platé, Alkaline hydrolysis of polyacrylonitrile. On the reaction mechanism, Macromol. Chem. Phys. 201 (2000) 2176–2180, https://doi.org/10.1002/1521-3935(20001101)201:16<2176::AID-MACP2176>3.0.CO;2-5.
[32] S. Lagergren, About the theory of so-called adsorption of soluble substances, K. Sven. VETENSKAPSAKADEMIENS Handl. 24 (1898) 1–39.
[33] Y.S. Ho, G. McKay, Pseudo-second order model for sorption processes, Process Biochem. 34 (1999) 451–465, https://doi.org/10.1016/S0032-9592(98)00112-5.
[34] Walter J. Weber, J. Carrell Morris, Kinetics of adsorption on carbon from solution, J. Sanit. Eng. Div. 89 (1963) 31–60.
[35] A. Pholosi, E.B. Naidoo, A.E. Ofomaja, Intraparticle diffusion of Cr(VI) through biomass and magnetite coated biomass: a comparative kinetic and diffusion study, south african, J Chem. Eng. 32 (2020) 39–55, https://doi.org/10.1016/J.SAJCE.2020.01.005.
[36] S. Çavuş, G. Yaşar, Y. Kaya, Z.B. Gönder, G. Gürdağ, İ. Vergili, Synthesis and characterization of gel beads based on ethyleneglycol dimethacrylate and 2-acrylamido-2-methyl-1-propane sulfonic acid: removal of Fe(II), Cu(II), Zn(II), and Ni(II) from metal finishing wastewater, Process Saf. Environ. Prot. 103 (2016) 227–236, https://doi.org/10.1016/J.PSEP.2016.07.011.
[37] H. Cheng, Y. Liu, X. Li, Adsorption performance and mechanism of iron-loaded biochar to methyl orange in the presence of Cr6+ from dye wastewater, J. Hazard. Mater. 415 (2021), 125749, https://doi.org/10.1016/j.jhazmat.2021.125749.
[38] G.R. Quezada, R.I. Jeldres, P.D. Fawell, P.G. Toledo, Use of molecular dynamics to study the conformation of an anionic polyelectrolyte in saline medium and its adsorption on a quartz surface, Miner. Eng. 129 (2018) 102–105, https://doi.org/10.1016/J.MINENG.2018.09.025.
[39] I. Langmuir, The adsorption of gases on plane surfaces of glass, mica and platinum, J. Am. Chem. Soc. 40 (1918) 1361–1403, https://doi.org/10.1021/ja02242a004.
[40] H. Freundlich, Über die Adsorption in Lösungen (Concerning adsorption in solutions), Chemie–Stochiometrie, Zeitschrift Fur Phys. 57 (1906) 385–490.
[41] P.H. Emmett, J.T. Kummer, Kinetics of ammonia synthesis, Ind. Eng. Chem. (1943), https://doi.org/10.1021/ie50402a012.
[42] M. Silva Da Rocha, K. Iha, A.C. Faleiros, E.J. Corat, M.E.V. Suárez-Iha, Henry's law as a limit for an isotherm model based on a statistical mechanics approach, J. Colloid Interface Sci. 208 (1998) 211–215, https://doi.org/10.1006/jcis.1998.5779.
[43] V.O. Shikuku, C.O. Kowenje, F.O. Kengara, Errors in parameters estimation using linearized adsorption isotherms: sulfadimethoxine adsorption onto kaolinite clay, Chem. Sci. Int. J. 23 (2018) 1–6, https://doi.org/10.9734/csji/2018/44087.
[44] A. Bonilla-Petriciolet, D.I. Mendoza-Castillo, H.E. Reynel-Ávila, Adsorption processes for water treatment and purification (2017), https://doi.org/10.1007/978-3-319-58136-1.
[45] J. Wang, X. Guo, Adsorption isotherm models: classification, physical meaning, application and solving method, Chemosphere 258 (2020), 127279, https://doi.org/10.1016/j.chemosphere.2020.127279.
[46] J.T. Martins, C.H. Guimarães, P.M. Silva, R.L. Oliveira, P. Prediger, Enhanced removal of basic dye using carbon nitride/graphene oxide nanocomposites as adsorbents: high performance, recycling, and mechanism, Environ. Sci. Pollut. Res. 283 (28) (2020) 3386–3405, https://doi.org/10.1007/S11356-020-10779-Z, 2020.
[47] U. Kamran, H.N. Bhatti, S. Noreen, M.A. Tahir, S.J. Park, Chemically modified sugarcane bagasse-based biocomposites for efficient removal of acid red 1 dye: kinetics, isotherms, thermodynamics, and desorption studies, Chemosphere 291 (2022), 132796, https://doi.org/10.1016/J.CHEMOSPHERE.2021.132796.
[48] P. Prediger, M.G.A. Vieira, N.G. Camparotto, T. de Figueiredo Neves, P.M.M. da Silva, G. de Vargas Brião, Adsorption and desorption aspects of carbon-based nanomaterials: recent applications for water treatments and toxic effects, Liq. Cryst. Nanomater. Water Pollut. Remediat. (2022) 59–87, https://doi.org/10.1201/9781003091486-4.
[49] S. Nausheen, H.N. Bhatti, Z. Furrukh, S. Sadaf, S. Noreen, Adsorptive removal of drimarine red HF-3D dye from aqueous solution using low-cost agricultural waste: batch and column study adsorptive removal of drimarine red HF-3D dye from aqueous solution using low-cost agricultural waste: batch and column study, Chem. Ecol. 30 (2014) 376–392, https://doi.org/10.1080/02757540.2013.861825.
[50] A.M. Kamil, F.H. Abdalrazak, A.F. Halbus, F.H. Hussein, Adsorption of Bismarck Brown R dye onto multiwall carbon nanotubes, J. Environ. Anal. Chem. 01 (2014) 1–6, https://doi.org/10.4172/2380-2391.1000104.
[51] P. Sun, S. Deore, A. Navrotsky, Formation and dehydration enthalpy of ion exchanged zeolite beta, Microporous Mesoporous Mater. 91 (2006) 15–22, https://doi.org/10.1016/J.MICROMESO.2005.11.018.
[52] M.P. Shah, Bioremediation of Azo Dye, Microb, Wastewater Treat. (2019) 103–126, https://doi.org/10.1016/B978-0-12-816809-7.00006-3.
[53] M. Clark, Fundamental principles of dyeing, Handb. Text. Ind. Dye. Princ. Process. Types Dye. 1 (2011) 3–27, https://doi.org/10.1533/9780857093974.1.1.
[54] C.Breno Rodrigues dos Santos, C.Carvalho Lobato, M.Alexandre Costa de Sousa, W. Jorge da Cruz Macêdo, J.Carlos Tavares Carvalho, Molecular modeling: origin, fundamental concepts and applications using structure-activity relationship and quantitative structure-activity relationship, Rev. Theor. Sci. 2 (2013) 1–25, https://doi.org/10.1166/rits.2014.1016.
[55] Z. Shariatinia, S. Shahidi, A DFT study on the physical adsorption of cyclophosphamide derivatives on the surface of fullerene C60 nanocage, J. Mol. Graph. Model. 52 (2014) 71–81, https://doi.org/10.1016/J.JMGM.2014.06.001.
[56] C.T. Zeyrek, S.B. Koçak, H. Ünver, S. Pektaş, N.S. Başterzi, Ö. Çelik, Molecular structure and density functional modelling studies of 2-[(E)-2-(4-hydroxyphenyl) ethyliminomethyl]phenol, J. Mol. Struct. 1100 (2015) 570–581, https://doi.org/10.1016/J.MOLSTRUC.2015.07.068.
[57] A. El Nemr, A.A. Moneer, A. Khaled, A. El Sikaily, G.F. El-Said, Modeling of synergistic halide additives' effect on the corrosion of aluminum in basic solution containing dye, Mater. Chem. Phys. 144 (2014) 139–154, https://doi.org/10.1016/J.MATCHEMPHYS.2013.12.034.
[58] M. Miar, A. Shiroudi, K. Pourshamsian, A.R. Oliaey, F. Hatamjafari, Theoretical investigations on the HOMO–LUMO gap and global reactivity descriptor studies, natural bond orbital, and nucleus-independent chemical shifts analyses of 3-phenylbenzo[d]thiazole-2(3H)-imine and its para-substituted derivatives: Solvent and substituent effects 45 (2020) 147–158, https://doi.org/10.1177/1747519820932091, 10.1177/1747519820932091.
[59] R.G. Parr, R.G. Pearson, Absolute hardness: companion parameter to absolute electronegativity, J. Am. Chem. Soc. 105 (2002) 7512–7516, https://doi.org/10.1021/JA00364A005.
[60] P.K. Chattaraj, U. Sarkar, D.R. Roy, Electrophilicity index, Chem. Rev. 106 (2006) 2065–2091, https://doi.org/10.1021/CR040109F.
[61] R.G. Pearson, Chemical hardness and the electronic chemical potential, Inorganica Chim. Acta. 198–200 (1992) 781–786, https://doi.org/10.1016/S0020-1693(00)92423-X.
[62] P. Mazumdar, D. Choudhury, Study of the alkyl- π interaction between methane and few substituted pyrimidine systems using DFT, AIM and NBO calculations, Comput. Theor. Chem. 1208 (2022), 113560, https://doi.org/10.1016/j.comptc.2021.113560.
[63] O. Gereben, L. Pusztai, Hydrogen bond connectivities in water–ethanol mixtures: on the influence of the H-bond definition, J. Mol. Liq. 220 (2016) 836–841, https://doi.org/10.1016/J.MOLLIQ.2016.05.035.
[64] T.N. Magalhães de Paula, J.A. Souza Vendemiatti, N.G. Camparotto, B. Toledo, Á. C. Oliveira, T.F. Neves, G.A. Umbuzeiro, P. Prediger, Behavior of two classes of organic contaminants in the presence of graphene oxide: ecotoxicity, physicochemical characterization and theoretical calculations, Sci. Total Environ. 822 (2022), 153515, https://doi.org/10.1016/J.SCITOTENV.2022.153515.
[65] Y. Yamazaki, J. Naganuma, H. Gotoh, A theoretical, dynamical evaluation method of the steric hindrance in nitroxide radicals using transition states of model reactions, Sci. Reports 91 (9) (2019) 1–11, https://doi.org/10.1038/s41598-019-56342-w, 10.1177/1747519820932091.
[66] M.Z. Çetin, P. Camurlu, An amperometric glucose biosensor based on PEDOT nanofibers, RSC Adv. 8 (2018) 19724–19731, https://doi.org/10.1039/C8RA01385C.
[67] M. Iqbal, A. Saeed, S.I. Zafar, FTIR spectrophotometry, kinetics and adsorption isotherms modeling, ion exchange, and EDX analysis for understanding the mechanism of Cd2+ and Pb2+ removal by mango peel waste, J. Hazard. Mater. 164 (2009) 161–171, https://doi.org/10.1016/J.JHAZMAT.2008.07.141.
[68] Q. Yao, B. Fan, Y. Xiong, C. Jin, Q. Sun, C. Sheng, 3D assembly based on 2D structure of Cellulose Nanofibril/Graphene Oxide Hybrid Aerogel for Adsorptive Removal of Antibiotics in Water, Sci. Reports 2017 71 7 (2017) 1–13, https://doi.org/10.1038/srep45914.
[69] J. Zheng, L. Xia, S. Song, Electrosorption of Pb(ii) in water using graphene oxide-bearing nickel foam as the electrodes, RSC Adv. 7 (2017) 23543–23549, https://doi.org/10.1039/C7RA02956J.
[70] H. Lv, H. Zhang, G. Ji, H. Lv, H. Zhang, G. Ji, Development of novel Graphene/g-C3N4 composite with broad-frequency and light-weight features, Part. Part. Syst. Charact. 33 (2016) 656–663, https://doi.org/10.1002/PPSC.201600065.
[71] A. Majumdar, S.C. Das, T. Shripathi, R. Hippler, Chemical synthesis and surface morphology of amorphous hydrogenated carbon nitride film deposited by N2/CH4 dielectric barrier discharge plasma 19 (2012) 161–170, https://doi.org/10.1080/15685543.2012.699751, doi:10.1080/15685543.2012.699751.
[72] N.U.M. Nizam, M.M. Hanafiah, E. Mahmoudi, A.W. Mohammad, A.A. Oyekanmi, Effective adsorptive removal of dyes and heavy metal using graphene oxide based pre-treated with NaOH / H2SO4 rubber seed shells synthetic graphite precursor: equilibrium isotherm, kinetics and thermodynamic studies, Sep. Purif. Technol. 289 (2022), 120730, https://doi.org/10.1016/J.SEPPUR.2022.120730.
[73] G. Xiong, Q. Zhang, B. Ren, L. You, F. Ding, Y. He, X. Fan, N. Wang, Y. Sun, Highly efficient and selective adsorption of cationic dyes in aqueous media on microporous hyper crosslinked polymer with abundant and evenly dispersed

sulfonic groups, ChemistrySelect. 5 (2020) 6541–6548, https://doi.org/10.1002/SLCT.202000927.
[74] G. Xiong, B.-B. Wang, L.-X. You, B.-Y. Ren, F.D. Yong-Ke He, I. Dragutan, V. Dragutan, Y.-G. Sun, Hypervalent silicon-based, anionic porous organic polymers with solid microsphere or hollow nanotube morphologies and exceptional capacity for selective adsorption of cationic dyes, J. Mater. Chem. 7 (2019) 5628–5641, https://doi.org/10.1039/c3ta10518k.
[75] M. Khosravi, B. Yahyaei, S. Azizian, Adsorption of Bismarck Brown by iron oxide nanosphere and its modified form, J. Dispers. Sci. Technol. 35 (2014) 1135–1142, https://doi.org/10.1080/01932691.2013.833484.
[76] J. Mittal, V. Thakur, A. Mittal, Batch removal of hazardous azo dye Bismark Brown R using waste material hen feather, Ecol. Eng. 60 (2013) 249–253, https://doi.org/10.1016/j.ecoleng.2013.07.025.
[77] U. Filipkowska, J. Rodziewicz, Analysis of the sorption efficiency of acid, basic and direct dyes using chitosan, fly ashes immobilized onto chitosan and modified sawdust immobilized onto chitosan as sorbents, Adsorpt. Sci. Technol. 30 (2012) 461–471, https://doi.org/10.1260/0263-6174.30.6.461.